Perovskite: scintillators, direct detectors, and X-ray imagers

Atanu Jana,[a] Sangeun Cho,[a] Supriya A. Patil,[b] Abhishek Meena,[a] Yongcheol Jo,[a] Vijaya Gopalan Sree,[a] Youngsin Park,[c] Hyungsang Kim,*,[a] Hyunsik Im*,[a] and Robert A. Taylor[d]

[a] Division of Physics and Semiconductor Science, Dongguk University, Seoul 04620, Republic of Korea. Email: *hskim@dongguk.edu (H.K.), hyunsik7@dongguk.edu (H.I.)*

[b] Department Nanotechnology & Advanced Materials Engineering, Sejong University, Seoul-05006, South Korea

[c] Department of Chemistry, School of Natural Science, Ulsan National Institute of Science and Technology (UNIST), Ulsan 44919, Korea

[d] Clarendon Laboratory, Department of Physics, University of Oxford, Parks Road, Oxford OX1 3PU, UK.

Abstract

Halide perovskites (HPs) are used in various applications, including solar cells, light-emitting diodes, lasers, and photodetectors. These materials have recently received a great deal of attention as high-energy radiation detectors and scintillators due to their excellent light yield, mobility-lifetime product ($\mu\tau$), and X-ray sensitivity. In addition, due to their solution-processability and low cost, perovskite materials could be used to produce thick perovskite films across wide areas, allowing for low-dose X-ray imaging. Perovskite-based scintillators and detectors could eventually replace commercialized products like thallium-doped cesium iodide (CsI:Tl) and amorphous silicon (Si). Here, we review all of the key properties of HPs, the relevant terminology necessary for radiation detection and scintillation, the physical mechanisms underlying their operation, the fabrication process, and perovskite crystals and thin-films of varying dimensionality used for high-energy radiation detection. We also cover the critical issues and solutions that HPs as detectors, scintillators, and imagers face.

1. Introduction

A scintillator is a type of phosphor material that converts various kinds of high-energy radiation (e.g. (a) electromagnetic (EM) radiation: X-rays/gamma rays (γ-rays) and (b) particle radiation: alpha rays (α-rays), beta rays (β-rays), electron rays, proton rays, heavy particle rays, neutron rays, etc.) into ultraviolet-visible (UV-Vis) light [1,2]. Then, photomultiplier tubes (PMTs), thin-film phototransistor (TFT) arrays, amorphous Si photodiodes (PDs), complementary metal-oxide semiconductor (CMOS) detectors, Si avalanche PDs (APDs), and arrays, or charge-coupled devices (CCDs) are used to detect the emitted light without damaging the detector. The EM radiation spans a broad range in which visible light falls in a small zone (400-800 nm). Visible light can be seen with the naked eye, but invisible rays, such as α-, β-, γ-, and X-rays cannot. To detect these rays, photographic plates possess a significant disadvantage due to their poor capability to absorb the radiation. Therefore, other detection methods are currently required urgently. There are different kinds of scintillators, such as organic crystal (e.g., stilbene and anthracene) [3,4], organic liquid (e.g. 2,5-diphenyloxazole (PPO)) [5], inorganic crystal (e.g., cesium iodide, gadolinium silicate, and gadolinium oxysulfide (GOS)) [6], gases (e.g., xenon and helium) [7], and plastic scintillator (e.g., polyvinyltoluene and polystyrene) [8]. These scintillators are used selectively depending on the radiation type and application purpose. Semiconductor-based conventional X-ray direct detectors, which convert X-ray photons into electrons, have superior resolution, much higher than scintillators. Unfortunately, direct detectors that use amorphous selenium, take longer to collect an image due to their lower X-ray stopping power and insufficient charge transport ability. Scintillator imagers, however, are more sensitive than direct X-ray imagers. In this case, the X-ray image quality is poor because of the lower conversion efficiency and the scattering-induced optical crosstalk. The typical synthesis of conventional scintillators, requires high-temperature sintering, producing agglomerated powders or bulk crystals that are difficult to process for device fabrication, whereas solution-processed scintillators are highly promising. Therefore, there is an imperative for the development of both direct and indirect detectors that can be synthesized at low temperatures.

Recently, lead HP scintillators and direct detectors in the form of single crystals (SCs), polycrystalline materials, and nanocrystals (NCs) have attracted great interest due to their tunable emission wavelength, low detection limit, high stopping power, and ease of fabrication, and the high atomic number of lead [9–13]. All the major breakthroughs using perovskites as scintillators and direct detectors are listed in **Table 1**.

Table 1. Breakthroughs in perovskite scintillator and detector research

Principal investigator *et al.*	Perovskite scintillator, detector and imager	Year
Vasil'ev	$CsPbCl_3$: X-ray scintillator	1995[14]
Asai	$(C_6H_{13}NH_3)_2PbI_4$: proton scintillator	2002[15]
Asai	3D and 2D hybrid perovskites: proton scintillator	2004[16]
Koshimizu	$(C_6H_5(CH_2)_2NH_3)_2PbBr_4$: γ-ray scintillator	2008[17]
Kanatzidis	$CsPbBr_3$ SCs: X-ray detector	2013[18]
Heiss	$MAPbI_3$: X-ray detector	2015[19]
Huang	$MAPbBr_3$ SCs: X-ray detector	2016[20]
Kovalenko	$MAPbI_3$, $FAPbI_3$ and I-treated $MAPbBr_3$: γ-ray detector	2016[21]
Soci	$MAPbI_3$, $MAPbBr_3$, and $(EDBE)PbCl_4$: X-ray scintillator	2016[22]
Kovalenko	$Cs_xFA_{1-x}PbI_{3-y}Br_y$ ($x = 0$–0.1, $y = 0$–0.6) SCs: γ-ray dosimetry	2017[23]
Huang	$MAPbBr_3$ SCs: X-ray detector	2017[24]
J. Matt	$MAPbI_3$ wafer: X-ray detector	2017[25]
Huang	$CH_3NH_3PbBr_{3-x}Cl_x$ SCs: γ-ray detector	2017[26]
Park	$MAPbI_3$ + $MAPbBr_3$ thin-film: X-ray detector and imager	2017[27]
Tang	$Cs_2AgBiBr_6$ SCs: X-ray detector	2017[28]
Kanatzidis	$CsPbBr_3$ SCs: γ-ray detector	2018[29]
Liu	$CsPbX_3$ (X = Cl, Br, I) NCs: X-ray scintillator	2018[30]
Tang	Rb_2CuBr_3 SCs: X-Ray scintillator	2019[31]
Brovelli	Plastic scintillator [$CsPbBr_3$ NCs + polymer + organic dye]; X-rays and α-particle scintillator	2020[32]
Im	$CsPbX_3$ (X = Cl, Br, I) NCs + PPO: X-ray scintillator and imager	2020[33]

Even though perovskites perform exceptionally well in direct and indirect detectors, many questions remain unanswered. How can we improve the light yield of perovskite materials? What is the structural-property relationship under high-energy radiation? How can we improve the X-ray image quality using perovskite-based detectors and scintillators? In this regard, we review the scintillation and luminescence properties of different types of perovskite materials irradiated with X-rays, γ- rays, α-rays, β-rays, and neutron rays. Though there have been some previous review papers on both direct and indirect perovskite X-ray detectors for imaging [34–39], we present various breakthroughs in perovskite scintillator and detector research over time, with a detailed explanation of the related terminology, the performance of common scintillators and direct X-ray detectors, direct and indirect X-ray detectors based on different dimensional perovskites and finally, we discuss gigahertz X-ray imaging and possible strategies to enhance the performance of perovskite X-ray detectors.

2. High-energy radiation sources (α-, β-, γ-, and X-rays) and their importance in various fields

The EM spectrum includes a wide range of radiation, including α-, β-, γ-, and X-rays. X-rays can be classified as "soft", with energies typically below 10 keV, or "hard", with energies ranging from 10 to 200 keV [40]. Today, X-rays are used in various fields such as crystallography, medical imaging, airport security, and microscopy. γ-ray photons are the most energetic photons in the EM spectrum. γ-ray photons generally exceed 100 keV. Because of their high penetration power, γ-rays can pass through many materials, including human tissue. γ-rays have substantially higher energy and penetrating ability than X-rays. Different radioisotope sources are used for generating γ-rays, such as ^{24}Na, ^{28}Al, ^{38}Cl, ^{56}Mn, ^{72}Ga, ^{76}As, ^{88}Y, ^{124}Sb, ^{140}La,^{144}Pr [1]. α-particles, also known as α-rays or α-radiation, consist of two protons and two neutrons bound together into a particle identical to a helium-4 nucleus. These charged particles [41] are used in scientific research, medical imaging, and environmental analysis. Various radioisotope sources are used for generating α-rays, such as ^{148}Gd, ^{232}Th, ^{238}U, ^{235}U, ^{236}U, ^{230}Th, ^{234}U, ^{231}Pa, ^{239}Pu, ^{243}Am [1]. The β-ray, which has moderate penetrating power, is a useful resource for monitoring surface radiative pollution. High-Z (atomic number) elements are suitable for X/γ-ray absorption, whereas light elements are better used as β-ray scintillators [42,43]. Various nuclides are used for generating β-rays such as ^{3}H, ^{14}C, ^{32}P, ^{35}S, ^{36}Cl, ^{45}Ca, ^{63}Ni, ^{90}Sr, ^{99}Tc, ^{147}Pm, ^{22}Na, ^{60}Co, ^{137}Cs.

3. Terms related to scintillation and radiation detection

3.1. Radioactivity: Radioactivity is the amount of ionizing radiation emitted by a substance. The standard international (SI) unit of radioactivity is the becquerel (abbreviated Bq), which equals 1 disintegration per second (dps). Another unit of radioactivity is the curie, a historical unit based on the number of dps in 1gram of radium-226 (37 billion disintegrations per second). One curie = 37 billion Bq, 1 picocurie (a trillionth of a curie) equals 0.037 Bq, and 1 Bq equals 27 picocuries. Radioactivity is also measured in disintegrations per minute (dpm) where 1 dpm equals 1/60 Bq.

3.2. Exposure: Exposure refers to the amount of ionization caused by radiation passing through air. The exposure units are roentgen (R) and coulomb/kilogram (C/kg). The amount of radiation required to generate a charge of 2.58×10^{-4} C in 1 kg of dry air is 1R.

3.3. Dose: Dose is the amount of radiation absorbed by a specific substance. The SI unit for absorbed dose is gray (Gy) or J/kg, where 1Gy is defined as the amount of radiation that results in 1 J energy absorption per kg of a specific substance. Gray is a measure of the energy deposited in tissue. Dose absorbed by dry air (Gy_{air}) can be converted to R using $1Gy_{air} = 114$ R. One gray is equal to 100 rads. Dose rate equals the amount of dose per unit time. The correlation between these units is as follows: 1 rad = 0.01 Gy = 0.01 J/kg = 100 erg/g.

3.4. Dose equivalent: Dose equivalent is expressed in terms of both the amount of radiation absorbed and the medical effects of a particular type of radiation. Units for dose equivalent are the roentgen equivalent man (rem) and sievert (Sv), and biological dose equivalents are commonly measured in 1/1000th of a rem (known as a millirem or mrem). The correlation between these units is as follows: 1 R (exposure) = 1 rad (absorbed dose) = 1 rem or 1000 mrem (dose equivalent). The more modern sievert = 100 rem. It is a large dose and is often seen in units of millisieverts (mSv) or microsieverts (μSv).

3.5. Kinetic energy released per unit mass (KERMA): KERMA is the sum of the initial kinetic energies of all charged particles released by uncharged ionizing radiation in a substance, divided by its mass. The gray (Gy) or joule per kilogram is the SI unit of KERMA, and it is the same as the unit of absorbed dose.

3.6. Unit of sensitivity: The unit of sensitivity is expressed in microcoulombs per air KERMA of milligray per square centimetre (μC $\mathrm{mGy_{air}}^{-1}$ cm^{-2}).

4. What are the important parameters for scintillators and detectors?

4.1 Scintillation parameters

4.1.1 Scintillation yield

The scintillation yield (or light yield) is the number of photons (N_{ph}) emitted by a scintillator per unit energy, deposited by ionizing radiation or with a γ-ray of quantum energy in the medium. Hence, it can be calculated using the following formula: $N_{\mathrm{ph}} = N_{\mathrm{eh}}SQ = \frac{E_\gamma}{E_{eh}}SQ$, N_{eh} is the number of electron-hole pairs, E_{eh} is the average energy necessary to produce one thermalized e-h pair, S is the transport/transfer efficiency of the e-h pair energy to the luminescence centre, and Q is the quantum yield for the final luminescence process. The components of the scintillation yield (conversion efficiency, transport, luminescence yield, and light collection) are, to some extent, all dependent on the structural quality of the lattice [44,45]. Scintillation properties of commonly used materials are listed in **Table 2**.

Table 2. Radioluminescence (RL) and light yield for commonly used scintillator materials.

Sl no	Material	Emission peak (nm)	Light yield (ph/MeV)	Ref.
1	BGO ($Bi_4Ge_3O_{12}$)	480	8,500	[46]
2	LYSO(Ce) [$Lu_{1.8}Y_{0.2}SiO_5$:Ce]	420	29000	[47]
3	CsI(Tl)	540-550	65,000	[46,48,49]
4	LiI(I)	470	11,000	[1]
5	NaI(Tl)	415	38,000–55,000	[1]
6	$CdWO_4$	470	15,000	[50–52]
7	$LaBr_3$ (Ce)	380	63,000	[53]
8	$LaBr_3$(5%Ce)	380	66,000	[54]
9	$CeBr_3$	380–390	57,000–66,000	[54]

10	YAP	370	17,000	[46,55]
11	GAGG(Ce) [$Gd_3Al_2Ga_3O_{12}$:Ce]	520	46000	[47]
12	CsI(Na)	420	38,500	[56]
13	YAG	550	16,400	[46]
14	CaF_2 (Eu)	435	24,000	[1]
15	SrI_2 (Eu)	435	85,000	[57]

4.1.2 Radioluminescence spectrum

Radioluminescence (RL) is is the wavelength (λ_{sc}) or frequency (ν_{sc}) distribution of the scintillation light when the medium is excited by ionizing radiation. It is mainly composed of a series of emission bands, and each of them is characterized by the maximum λ_{sc} or ν_{sc} and half-width $\Delta\lambda_{sc}$ ($\Delta\nu_{sc}$) at a given temperature.

4.1.3 Energy resolution

The energy resolution (R) of the scintillation detector is one of the most important parameters for distinguishing between different types of radiation [58]. The energy resolution value ($\Delta E/E$) is calculated by dividing the peak width at half maximum (ΔE) of the total peak in the pulse-amplitude spectrum by the peak position maximum (E). R can thus be defined as a function of various contributions: $R^2 = {R^2}_{np} + {R^2}_{lim} + {R^2}_{inh}$, where R_{np} is the factor of non-proportionality. In a few scintillators, the number of emitted photons is not proportional to the absorbed energies that lead to a distribution of the light yield, which deteriorates the value of R. The parameter R_{inh} is associated with the inhomogeneity of the crystal, inducing local variations in the light efficiency. Therefore, it is essential to synthesize defect-free crystals that will exhibit better reflecting properties. The parameter R_{lim} is the ultimate or statistical resolution of the perfect detector, and it is determined by the Poisson's law: $R_{lim} = 2.35\sqrt{\frac{1+v(PM)}{N_{phe}}}$, where ν(PM) denotes the variance of the photomultiplier (PM) gain and N_{phe} represents the number of photoelectrons emitted by the PM due to scintillation absorption by its photocathode [44,59,60].

4.1.4 Photon detector efficiency (PDE)

The photon detection efficiency (PDE) of a silicon photomultiplier (SiPM) is influenced by the wavelength of the incident light, the applied overvoltage, and the microcell fill factor. In particular, the product of the quantum efficiency (QE), the avalanche-initiation probability ($\mathcal{E}$), and the microcell fill factor (F) determine the PDE in a SiPM as follows:

$$\mathrm{PDE}(\lambda, V) = \mathrm{QE}(\lambda, V) \times \mathcal{E}(V) \times F$$

Crosstalk and afterpulsing can render the direct measurement of the PDE of a SiPM more difficult. To overcome these issues, the PDE is commonly estimated using the responsivity of the sensor (R), which is defined as the ratio of the measured photocurrent to the incident optical power at a particular wavelength. The PDE can be calculated using the following equation:

$$\mathrm{PDE} = (R.h.c)/(e \times \lambda \times G)(1 + P_{XT})(1 + P_{AP}),$$

where R is the responsivity, h is Planck's constant (6.626×10^{-34} m²kg s^{-1}), c is the speed of light (2.998×10^{8} m/s), e is the elementary charge (1.602×10^{-19} C), λ is the wavelength of the incident light, G is the gain, P_{XT} is the crosstalk probability, and P_{AP} is the afterpulsing probability.

4.2 Key parameters in high-energy radiation detectors

4.2.1 Ionization energy

The ionization energy of a scintillator is defined as the minimum energy required to create an e-h pair at the atomic level under high-energy radiation. According to the empirical model proposed by Klein [61], the ionization energy of semiconductor materials can be calculated as follows:

$$W_k = 2.8 \times E_g + E_{\text{phonon}}$$

where E_g and E_{phonon} are the bandgap and phonon energy term (0.5 – 1.0 eV) of the semiconductor material, respectively. This empirical formula, which is known as the Klein rule, posits a direct relationship between the ionization energy and the bandgap. In several cases, theoretical predictions using this formula closely match experimental values. For example, Nie *et al.*

calculated the experimental ionization energy (W_e) of 4.46 eV for a 2D-layered perovskite $(BA)_2(MA)_2Pb_3I_{10}$ material using the following equation:

$$W_e = \frac{\Phi \times E \times \eta}{\frac{Q}{q}}$$

where Φ is the photon flux (Ct s^{-1} cm^{-2}), E is the X-ray photon energy (eV), η is the absorption efficiency of the material, Q is the total charge density (C cm^{-2} s^{-1}), and q is the elementary charge [62]. According to the Klein rule, the predicated ionization energy of $(BA)_2(MA)_2Pb_3I_{10}$ is 5.54 eV, which is in good agreement with the experimental value.

4.2.2 Detector's sensitivity and signal-to-noise ratio (SNR)

The detector's sensitivity is the most important figure of merit to evaluate the performance of an X-ray detector for various imaging applications. It is defined as the collected charge Q per unit exposure to high-energy radiation per unit area [63,64]. The X-ray sensitivity (S) of a detector can be evaluated as follows: $S = \Delta I / DA$; where photocurrent $\Delta I = I_{\text{light}} - I_{\text{dark}}$, D is the dose rate of incident X-ray radiation, and A is the area of the detector [65].

The SNR measures the ratio between the level of a desired signal to the level of background noise in image processing. This factor plays a key role in determining the image quality of an X-ray detector. The SNR is further divided into two types: input SNR and output SNR [66]. The detective quantum efficiency (DQE) can be calculated from the following relation:

$$DQE = [SNR_{\text{out}} / SNR_{\text{in}}]^2.$$

4.2.3 Linear X-ray absorption coefficient

The absorption coefficient (μ_{ac}) is the sum of the mass fraction of all elements in the compound.

$$\mu_{ac} = \sum_i f_i \mu_i = \frac{\Sigma_i N_i A_i \mu_i}{\Sigma_i N_i A_i}$$

i denotes the elements of the compound, f_i is the mass fraction of element i, μ_i is the absorption coefficient of element i, N_i is the number of atoms of element i in the compound, and A_i is the atomic weight of element i [62]. For $CH_3NH_3PbBr_3$ (CNH_6PbBr_3), the absorption coefficient (μ_{ac}) can be calculated as follows:

$$\mu_{ac} = \frac{A_C\mu_C + A_N\mu_N + 6A_H\mu_H + A_{Pb}\mu_{Pb} + 3A_{Br}\mu_{Br}}{A_C + A_N + 6A_H + A_{Pb} + A_{Br}}$$

4.2.4 Mobility-lifetime product ($\mu\tau$)

The mobility-lifetime product ($\mu\tau$) is a key parameter, that evaluates the quality of semiconductor-based radiation detectors. $\mu\tau$ is directly correlated with the mean drift length $\lambda = \mu\tau E$ under an applied electric field E. In fact, the electrons and holes generated by the incident radiation must have a large enough λ to reach the electrodes before recombination. For elemental semiconductors, $\mu\tau$ is in the order of 1 $cm^2\ V^{-1}$ for electrons and holes, while for compound semiconductors, this value is typically in the order of 10^{-4} and 10^{-5} $cm^2\ V^{-1}$ for electrons and holes, respectively. Usually, a $\mu\tau$ product of $> 10^{-4}$ $cm^2\ V^{-1}$ is desirable for detector materials [67–69].

4.2.5 Charge collection efficiency (CCE)

The charge collection efficiency **(**CCE) is an important property of a detector, and it directly influences the performance, in particular, the energy resolution. CCE is the ratio of the electrical charge Q generated in the external circuit to the charge Q_0 generated by the incident radiation on the detector. CCE can be determined by the Hecht equation as follows:[64,70,71]

$$\mathrm{CCE} = \frac{Q}{Q_0} = \left[\frac{\lambda_h}{L}\left(1 - e^{-\frac{x}{\lambda_h}}\right) + \frac{\lambda_e}{L}\left(1 - e^{-\frac{L-x}{\lambda_e}}\right)\right],$$

where, L is the detector thickness, and $\lambda_h = \mu_h\tau_h E$ and $\lambda_e = \mu_e\tau_e E$ are the mean drift length of holes and electrons, respectively. Hence, CCE strongly depends on λ_h and λ_e, as well as the incoming photon interaction position x (i.e., the distance between the created electrons and holes and the electrodes). Note that under X-ray (or γ- ray) irradiation, the linear attenuation coefficient of the detector material has to be taken into account in the CCE equation [71].

Some commonly used radiation detectors with their physical properties have been listed in **Table 3.**

Table 3. Physical properties of some radiation detectors [72–74]

Material	Bandgap (eV)	Density	$(\mu\tau)_e$ ($cm^2\ V^{-1}$)	$(\mu\tau)_h$ ($cm^2\ V^{-1}$)
Si	1.12	2.33	>1	~1

Ge	0.67	5.33	>1	>1
a-Se	2.2	4.3	0.005×10^{-6}	0.0014×10^{-6}
TlBr	2.68	7.56	6.5×10^{-3}	$\sim 10^{-4}$
InP	1.35	4.78	5×10^{-6}	$<1.5 \times 10^{-5}$
GaAs	1.43	5.32	8×10^{-5}	4×10^{-6}
PbI_2	2.32	6.2	8×10^{-6}	9×10^{-7}
BiI_3	1.3	5.78	N/A	N/A
α-HgI_2	2.15	6.4	8×10^{-4}	3×10^{-5}
CdTe	1.44	5.85	3×10^{-3}	2×10^{-4}
CdZnTe	1.57	5.78	2.3×10^{-2}	2.4×10^{-5}
CdZnSe	2.0	5.5	$\sim 10^{-4}$	10^{-6}
CdMnTe	1.73	5.8	$>10^{-6}$	N/A
$Hg_3S_2I_2$	2.25	7.04	1.6×10^{-6}	N/A
$Hg_3Se_2I_2$	2.12	7.38	$\sim 1\times10^{-5}$	N/A
$Hg_3Te_2I_2$	1.93	7.58	3.3×10^{-6}	N/A
$Cs_2Hg_3S_4$	2.8	6.29	4.2×10^{-4}	5.82×10^{-5}
$Cs_2Hg_6S_7$	1.63	6.94	1.2×10^{-3}	1.0×10^{-4}
$TlGaSe_2$	1.93	6.4	6×10^{-5}	9.2×10^{-6}

4.2.6 Leakage currents

Leakage currents are generally determined by the electronic band structure of a detector material and device configuration. Actually, the leakage current largely depends on the intrinsic carrier concentration, which is determined by the band gap of the material [75]. Small band gap semiconductor-based detectors should operate at low temperatures to decrease the carrier concentration-dependent leakage current which is an electrical noise source that degrades detection efficiency and energy resolution [76]. Furthermore, impurities and defects can decrease the resistivity of the detector and increase the leakage current noise level [77].

4.2.7 Polarization effect

The term “polarization effect” was coined in the semiconductor detector industry to describe any long-term changes in system performance caused by applied bias. The electric field in the detector can be modified as a result of the polarization effect. As internal fields are created, this often shifts the effect of the applied external field. The CCE of the detector is reduced due to these internal fields. The polarization effect becomes more pronounced as detectors are damaged by radiation over time [70]. The polarization effect can be neutralized in detector materials via heating the detector, alternating the bias polarity, setting the bias off and waiting, illuminating the detector [78].

4.2.8 Gain factor

The gain factor (G) of a photoelectric detector can be calculated as follows:

$G = I_R / I_P$, where I_R is the measured current, and I_P is the theoretical current, $I_P = \varphi\beta e$. φ is the photon absorption rate (photons s^{-1}), and can be calculated as follows:

$$\varphi = \varepsilon D m_s / E_{ph},$$

where ε is the fraction of absorbed photons, D is the dose rate, m_s is the crystal mass, and E_{ph} is the X-ray energy. β is the maximum number of carriers generated by a photon and is determined by

$$\beta = E_{ph} / \Delta,$$

where Δ is the empirical ionization energy [61,79].

Therefore, the theoretical current I_P can be calculated using the following equation:

$$I_P = \varphi\beta e = \varepsilon D m_s e / \Delta.$$

4.3 Key parameters in X-ray imaging

Image quality can be described as the aspect of an image that influences a clinician's confidence in visualizing the right diagnostic features. Computed radiography (CR) and digital radiography (DR) are the most prevalent digital radiographic detectors. The significant components of radiography image quality are spatial resolution, noise, contrast, dynamic range, and artifacts [80]. These components are discussed briefly in this section.

4.3.1 Spatial resolution

Spatial resolution is a measure of scintillation performance that describes the ability to separate two points and is quantified as the smallest separation of two points that can be distinguished from each other. The most common method for measuring the spatial resolution is spatial frequency, defined as the number of details that can fit into a given space. The spatial frequency from a line-pair resolution test template can be used to calculate the spatial resolution. The spatial resolution is determined by counting cycles or line pairs per unit of distance (millimeters, inches, pixels, or image height). Line pairs per millimeter (lp/mm) is the most common spatial frequency unit, but for digital images, cycles/pixel (C/P) and line width/picture height (LW/PH) are more convenient [81].

4.3.2 Noise

Random or organized variations within a picture that do not correlate to X-ray attenuation variations of the object are referred to as radiographic noise. The noise power spectrum is the most accurate noise metric for determining the noise's spatial frequency content. Image noise is mostly caused by quantum noise, which is determined by the number of X-ray quanta employed to create the image. The great strategy to reduce quantum noise is to control exposure parameters.

4.3.3 Contrast

The signal or brightness difference between the structure of interest and its surroundings is referred to as radiographic contrast. Different tissues attenuate X-rays differently, creating contrast. The atomic number, density, and thickness of a tissue are all proportional to radiographic contrast. X-ray attenuation, for example, is lowest in air, highest in bone, and somewhere in between in soft tissues. The contrast in digital radiography can be altered using picture post-processing techniques, in which pixel values are changed to produce the desired range of contrast based on specific clinical requirements.

4.3.4 Dynamic range

The dynamic range refers to the range of X-ray intensity that the detector can image. To obtain high-quality digital radiographs, radiographic detectors that give good contrast over a wide dynamic range are required. Wide dynamic range detectors will display very low or very high exposure values in an image, allowing viewers to see various visual intensities. Although photographs with a narrow latitude have more visible contrast, extreme exposure intensities appear overly white or black with no discernible contrast.

4.3.5 Artifacts

Artifacts are caused by several factors such as uneven magnification, a non-uniform image due to detector issues, poor detector elements, aliasing, and inappropriate grid utilization, leading to poor image quality.

5. How do scintillators and detectors work

Depending on their operating mechanism, X-ray detectors can be indirect or direct. This chapter explains and addresses the detection mechanisms for indirect and direct X-ray detectors in detail. In addition, we summarize the key elements used to assess the efficiency of both detector types from a physical perspective.

5.1 Scintillation mechanisms

In the scintillation conversion process, three sub-processes occur (**Figure 1**):

(a) **Absorption/multiplication:** In the interaction between electromagnetic radiation and matter, three fundamental mechanisms are involved: photoelectric absorption, Compton scattering, and electron−positron pair formation. Photoelectric absorption is the dominant mechanism at low energy levels (i.e., up to a few hundred keV). However, Compton scattering becomes dominant at energies higher than a few hundred keV. In this situation, the incident high-energy photons only transfer a small portion of their energy, with the rest scattered by the outer shell electron. In photoelectric absorption, an inner shell hole and a primary electron are formed, causing the atom to become ionized. The multiplication of electrons and holes is the next step, which involves various complicated processes, including secondary X-ray, non-radiative decay (Auger processes), and inelastic electron/electron scattering. The mechanisms for e^+e^- pair formation can occur above a threshold of 1.02 MeV. In addition to photoelectric absorption and Compton scattering, electron−positron pair formation is favorable for high-Z materials. Electrons continue to lose energy mostly through Coulomb scattering below the threshold for electron−positron pair formation. These processes include a significant number of charge carriers with kinetic energies below the ionization threshold. Electrons and holes thermalize to the bottom of the CB and the top of the VB, respectively, at this stage. The entire process takes place on a sub-picosecond scale via carrier-carrier scattering.

(b) **Energy carrier transport:** At the site of incident radiation absorption and final emission, the radiation-generated electrons and holes do not interact or recombine. Until they transfer to a luminescence core, many electrons and holes first migrate within 10^{-12} to 10^{-8} s in the transport stage. Trap states are crucial at this point. If there are many trap states in a scintillation material, the scintillation process will be less efficient. Migrating charge carriers may be caught by defects such as ionic vacancies and grain boundaries in scintillator materials or become self-trapped in the crystal lattice, resulting in nonradiative losses and possible radiative recombination delays during the transport stage. These defects must be effectively suppressed by improving the crystal growth and/or surface morphology of the scintillation material. Large crack-free SCs will thus be extremely useful in enhancing scintillation performance.

(c) **Relaxation/emission:** The emission process, in which scintillation photons are emitted, is the final stage. The energy stored in an excited emitting center can be released in two ways: by emitting a photon or through non-radiative processes. Radiative photon emission can occur via the recombination of electrons and holes or the interaction of energetic secondary electrons with luminescent ions. These secondary electrons are highly effective if they reach as many luminescence centers as possible. Secondary electron dispersion has a spatial size of ~100 nm. There are around 10^9 atoms in an incoming radiation quantum of 1 MeV within a volume of 100 nm^3, and the number of secondary electrons is around 10^5. Direct electron−hole recombination is common in semiconductor-based scintillators such as ZnO and lead HPs. Activator-type scintillators, such as Ce-doped materials, on the other hand, rely heavily on the excitation of luminescent ions. The number of photons N_{ph} produced according to the energy of the incoming particle determines the overall conversion efficiency: $N_{ph} = N_{e/h}SQ = (E_{incident}/E_{e/h})SQ = (E_{incident}/\beta E_g)SQ$, where the number of electron−hole pairs generated during the multiplication stage, the efficiency with which an energy carrier can excite a luminescent center, and the QE of the luminescent center are represented by $N_{e/h}$, S, and Q, respectively. The energy of the incident particle and that required to create a thermalized electron−hole pair, respectively, are $E_{incident}$ and $E_{e/h}$. The bandgap of the material (E_g) with the proportional constant β (varying between 2 and 3) is equal to $E_{e/h}$. It is important to note that the scintillation mechanism described above only applies to inorganic scintillators; that for organic or non-crystalline scintillators can be more complicated.

5.2 Direct X-ray detection mechanism

A bulk semiconductor absorbs x-ray photons, forming a charge cloud in the material. Defect states can trap excited electrons (holes), allowing the holes to traverse between electrodes many times before recombination. To store and process the collected charges into signals, a thin-film transistor (TFT) or complementary metal oxide semiconductor (CMOS) array is required. The TFT-based flat panel detector (FPD) is widely used in X-ray imaging applications, such as optical radiography and mammography.

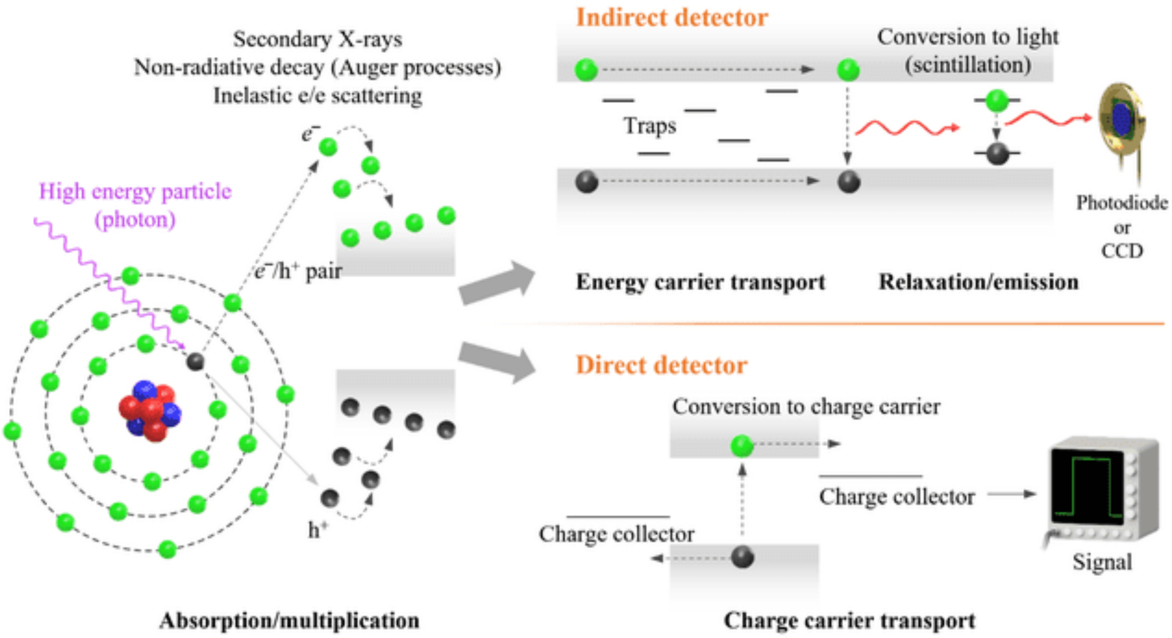

FIGURE 1. Mechanism of indirect detectors (scintillators) and direct detectors for high-energy radiation and particles.

6. Growth strategies for high-quality SCs

HP SCs have attracted the interest of researchers due to their ease of development and potential commercial use as scintillators and radiation detectors. Many methods for growing perovskite

SCs with various compositions, sizes, and exposed facets have been reported (**Figure 2**). The benefits of these approaches and their general processes are presented in this chapter.

6.1 Inverse temperature crystallization (ITC)

Bakr et al. proposed the ITC method to synthesize lead HP SCs [82]. The solubility of perovskite decreases in some solvents with increasing temperature. γ-butyrolactone (GBL), dimethyl sulfoxide (DMSO), and N, N-dimethylformamide (DMF) are suitable solvents for $MAPbI_3$, $MAPbCl_3$, and $MAPbBr_3$, respectively, whereas DMSO is the best solvent for growing inorganic $CsPbBr_3$ SCs using ITC. The growth temperature and precursor concentration heavily influence the quality and production yield of SCs. In ITC, large-sized crystals can be grown faster by introducing a crystal seed to the saturated precursor solution. This is attributed to the critical Gibbs free energy G* required for nucleation [83]. As a result, crystallization begins spontaneously from the seed. Otherwise, the crystal will spontaneously dissolve. Therefore, a crystal seed should be introduced to grow large, high-quality SCs. ITC is convenient for growing multi-component HP SCs such as $MA_xFA_{1-x}PbI_3$ SCs [84].

6.2 Anti-solvent vapor-assisted crystallization (AVC)

The AVC approach uses the solubility of the precursor solution in various solvents to generate high-quality SCs in a repeatable and temperature-independent manner. Bakr's group developed a method to generate crack-free $MAPbBr_3$ SCs with a volume of more than 100 mm^3 [85]. When a precursor is placed in a sealed bottle containing an antisolvent, the solubility drops as the antisolvent diffuses into the precursor solution, causing crystal formation. In general, solvents such as DMF, γ-butyrolactone (GBL), and DMSO should dissolve precursors, whereas $MAPbX_3$ SCs should be insoluble in antisolvents such as DCM, acetonitrile, and chlorobenzene (CB). With this approach, SCs produced with a $PbBr_2$/MABr molar ratio of 1.0 may change from transparent to opaque. This is attributed to the large difference in solubility between MABr and $PbBr_2$ in DMF. $PbBr_2$ precipitates faster than MABr after the antisolvent has consumed the majority of the DMF solvent, which could result in non-stoichiometric $MAPbBr_3$ or surface contaminants. Wei *et al*. employed a molar ratio of 0.8 to overcome this problem, ensuring that there was always more MABr than $PbBr_2$ in the solution [20]. This resulted in the formation of clear SCs (1–6 mm) that were used for the fabrication of X-ray detectors. All-inorganic $CsPbBr_3$ SCs were also prepared using the AVC approach [86]. The atomic usage efficiency of raw materials can be considerably improved using AVC, which is also useful for eliminating temperature-dependent phase transitions, convective current disturbances, and potential lattice disorder generated by MA^+ solvation during crystal formation because it does not require heat. However, AVC has the disadvantage of being difficult to scale up for industrial uses and it has lower reproducibility than other methods.

6.3 Bridgman growth

Perovskite precursors are heated in a silica tube for Bridgman growth above the melting point of precursors and held at that temperature for a longer time to avoid heterogeneous nucleation and suppress the formation of structural defects [29]. The ingot is then cooled slowly to room temperature. Cracks and the fracturing of the ingot are likely to result from an excessively high temperature gradient and a reduction in speed and cooling rate. Therefore, these parameters should be considered to obtain better-quality SCs that can be used as scintillators and detectors.

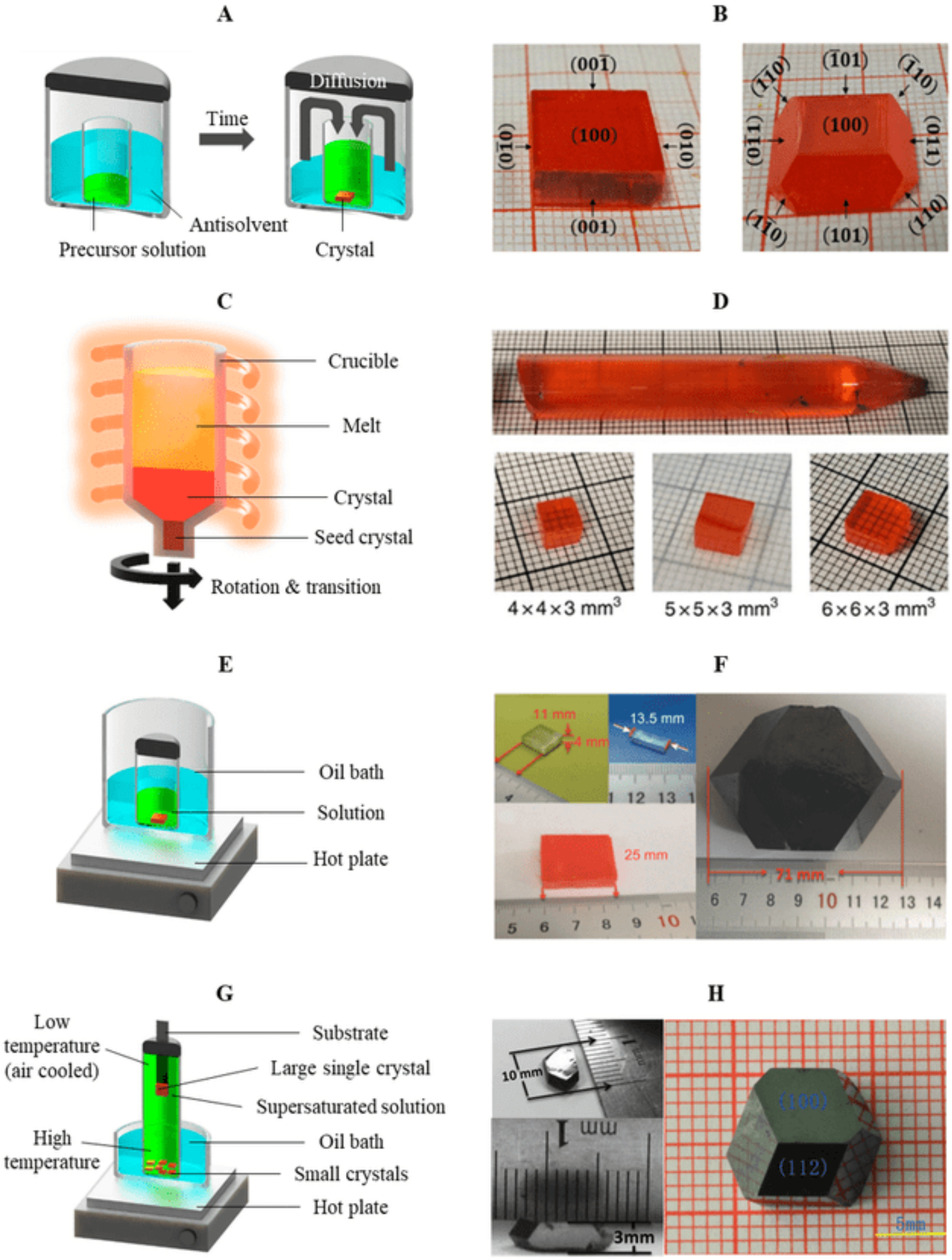

FIGURE 2. Various methods for synthesizing perovskite SCs. (A) the AVC method and (B) $MAPbBr_3$ SCs synthesized using AVC. Reproduced with permission [87]. (C) The Bridgman method and (D) $CsPbBr_3$ SCs fabricated using the Bridgman method. Reproduced with permission [29]. (E) The ITC method and (F) $MAPbX_3$ SCs (X =Cl or Br or I) produced using the ITC method. Reproduced with permission [88]. (G) The STL method and (H) $MAPbI_3$ SCs grown using the STL method. Reproduced with permission. Figure 3H (right) [89] and 3H (left) [90].

In the Bridgman method, raising the temperature above the melting point is helpful for raw materials with low solubilities, such as all-inorganic perovskites, despite the long growth time and significant energy consumption needed. However, this process necessitates using a particular Bridgman furnace, which limits its applicability.

6.4 Solution temperature lowering (STL)

Weber's methodology, which makes use of the variation in the solubility of the perovskite precursor in different solvents at varying temperatures, is the basis for the STL method. In this method, the precursors are dissolved in polar solvents at high temperatures and then slowly cooled to room temperature to obtain perovskite SCs. This process has been adopted to produce SCs that have been used in scintillators and detectors. In a typical example of the synthesis of $MAPbI_3$ SCs using STL, lead(II) acetate trihydrate and methylammonium iodide were combined in a hydriodic acid solution at 65 °C. When the temperature was reduced from 65 to 40 °C, the solution became saturated, and well-shaped $MAPbI_3$ SCs with 10 mm × 10 mm × 8 mm were produced [89].

7. Fabrication of samples for scintillation, radiation detection, and X-ray imaging

X-ray beams are extremely difficult to focus, diffract, or mirror in comparison to visible light, so large-area panels are needed for X-ray imaging. Metal HP (MHP)-based detectors can be easily rendered using various low-cost techniques, such as direct growth by solution processing on Si wafers, printing, conformal attachment, and isostatic pressing [91]. Herein, we discuss various sample fabrication methods for scintillation, direct radiation detection, and imaging.

7.1 Fabrication methods for scintillation and imaging

For indirect-type X-ray detectors, terbium-doped GOS (Gd_2O_2S:Tb) and CsI:Tl materials are commonly being used as a scintillator. Heo *et al*. developed a cost-effective $CsPbBr_3$ perovskite nanocrystal (PNC) scintillator and demonstrated high-performance detectors with high spatial resolution, sensitivity, and stability for indirect X-ray detectors. The $CsPbBr_3$ nanocrystal (NC) film was fabricated by spin coating on a glass substrate, and the obtained film was then directly paired with CMOS arrays and Si PDs (**Figure 3A, B**) [92]. The $CsPbBr_3$ NC-based X-ray detector exhibits superior spatial resolution (9.8 lp mm^{-1} at modulation transfer function (MTF) = 0.2 and 12.5–8.9 lp mm^{-1} for a linear line chart), a faster response time (~200 ns), and comparable stability compared to the commercialized GOS-based detectors. The solution processability of PNCs allows for the production of a thin-film scintillator device for ultrasensitive X-ray detection.

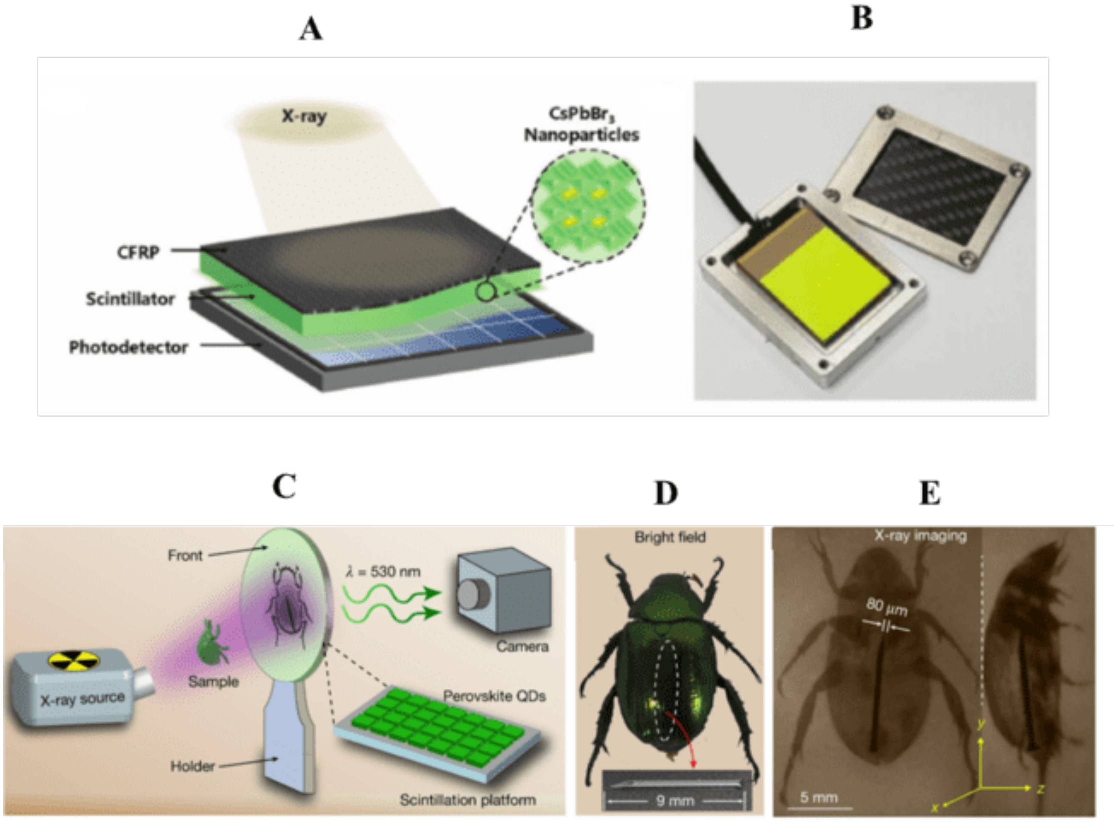

FIGURE 3. Fabrication of $CsPbBr_3$ NC-based X-ray detectors. (A) Schematic diagram of an X-ray detector configuration showing carbon fiber reinforced polymer (CFRP) film/scintillator film/arrayed Si-PDs module. (B) Photograph of $CsPbBr_3$ NCs integrated with Si-PDs-arrays for X-ray module. Reproduced with permission [92] (C) Experimental setup for real-time X-ray diagnostic imaging of biological samples. A beetle is placed between the X-ray source and a scintillation platform made of perovskite QDs. (D) and (E) Beetle's Bright-field and X-ray images, respectively, captured with a digital camera. Reproduced with permission [30].

Spin-coated $CsPbBr_3$ NCs are used for an X-ray sensing system, transforming high-energy X-ray photons into visible light that may be detected by a PMT. Chen *et al.* fabricated an X-ray scintillation detector by first covering a polydimethylsiloxane (PDMS) substrate with perovskite quantum dots (QDs) and then attaching a PMT for maximum visible photon collection (**Figure 3C-E**) [30]. Direct X-ray contrast imaging using high-efficiency PNCs is easily suited to high-throughput electronics inspection and tissue imaging, where standard digital cameras can be employed.

7.2 Fabrication methods for radiation detection

X-ray beams are very difficult to concentrate, diffract, and reflect, compared to the visible light, and panels with a large area are thus needed for X-ray beam imaging. MHP detectors can be fabricated easily through different low-cost methods, for example, direct growth through solution processing on Si wafers, printing, conformal attachment, and isostatic pressing. The solution-processed photodetector techniques such as doctor blading, inkjet printing, spin-coating, and spray-coating have many manufacturing advantages (such as ease of processing) and efficient performance for various applications [91]. Other scalable methods for MHP detectors have also been developed to improve their efficiency. Kim *et al.* [27] fabricated an 830 μm-thick polycrystalline $MAPbI_3$ (MPC) photoconductor layer sandwiched between polymer/perovskite composites, demonstrating high a μτ product of 1×10^{-4} cm^2 V^{-1} and good X-ray sensitivity of 11 μC mGy_{air}^{-1} cm^{-2} (**Figure 4**). Wei *et al.* [24] added a layer of brominated (3-aminopropyl) triethoxysilane (APTES) molecules to connect the MHP perovskite and Si wafers through primary chemical bonds. The APTES molecule binds with the native oxide (–OH) on the Si wafer via a condensation process to form strong covalent Si–O–Si bonds, and the APTES molecule assists in the perovskite crystal with its ammonium bromide group to prepare the Si-integrated $MAPbBr_3$ SC device using a low-temperature solution-processed molecular bonding method (**Figure 5**) [24].

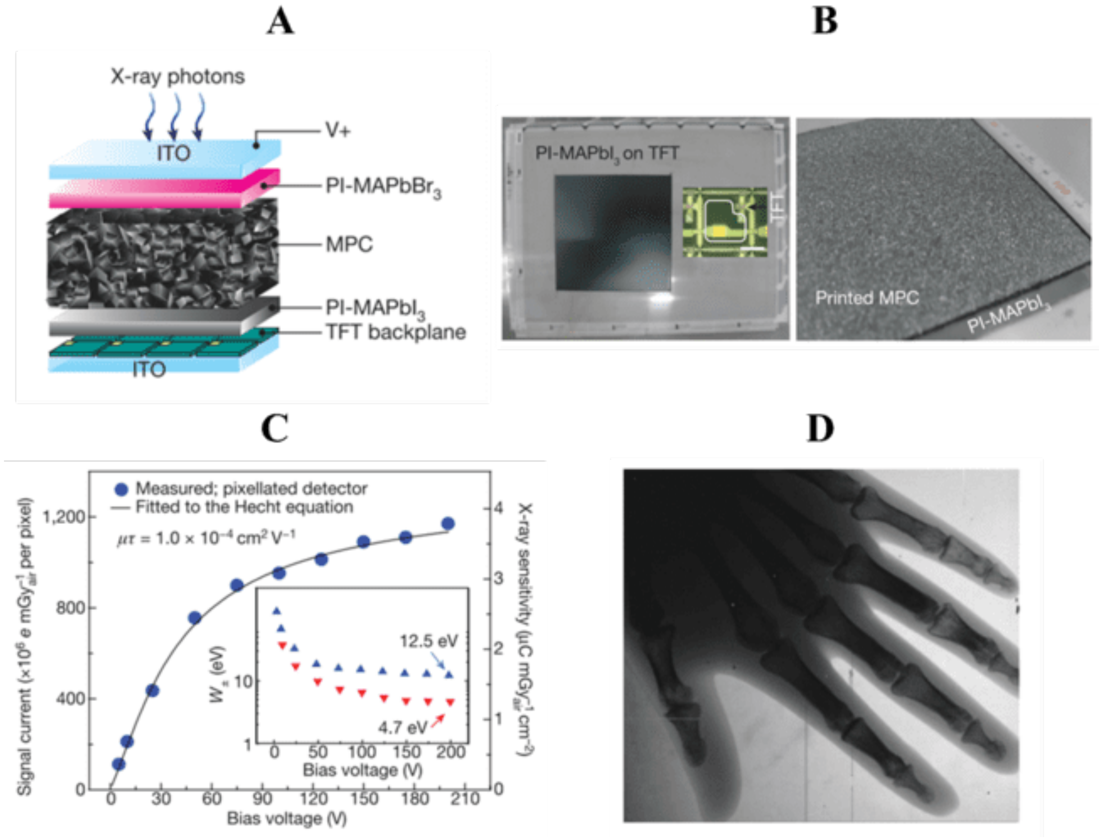

FIGURE 4. Hybrid perovskites are being used to create an X-ray detector. (A) All-solution-processed digital X-ray detector. (B) Spin-cast polyimide (PI)-MAPbI$_3$ on α-Si:H TFT backplane (left panel). Inset: Single-pixel structure of TFT (scale bar 30 μm). Printed MPCs on PI-MAPbI$_3$ (right panel). (C) Charge collection and sensitivity of MPC detector measured at 100 kVp. Inset: hole-h pair generation energy ($W\pm$) in the pixelated (blue triangles) and diode (red triangles) detectors. (D) Hand phantom X-ray image obtained using MPC detector. Reproduced with permission [27].

Yang *et al.* [93] used an isostatic-squeezing strategy to incorporate $Cs_2AgBiBr_6$ wafers with upscaling ability, fulfilling the criteria for a large-area imaging application. They used an isostatic-pressing method, which does not require a solvent during the $Cs_2AgBiBr_6$ film fabrication process and produces a highly compact and pinhole-free $Cs_2AgBiBr_6$ wafer. The $Cs_2AgBiBr_6$ crystals in the form of ball-milled powder were fitted into a pie-shaped mold through a compressor, and consequently, a pressure of 200 MPa was applied through a hydraulic press. Consequently, the device showed a remarkable sensitivity of 250 μC Gy_{air}^{-1} cm^{-2}, and a spatial resolution of 4.9 lp mm^{-1} [93].

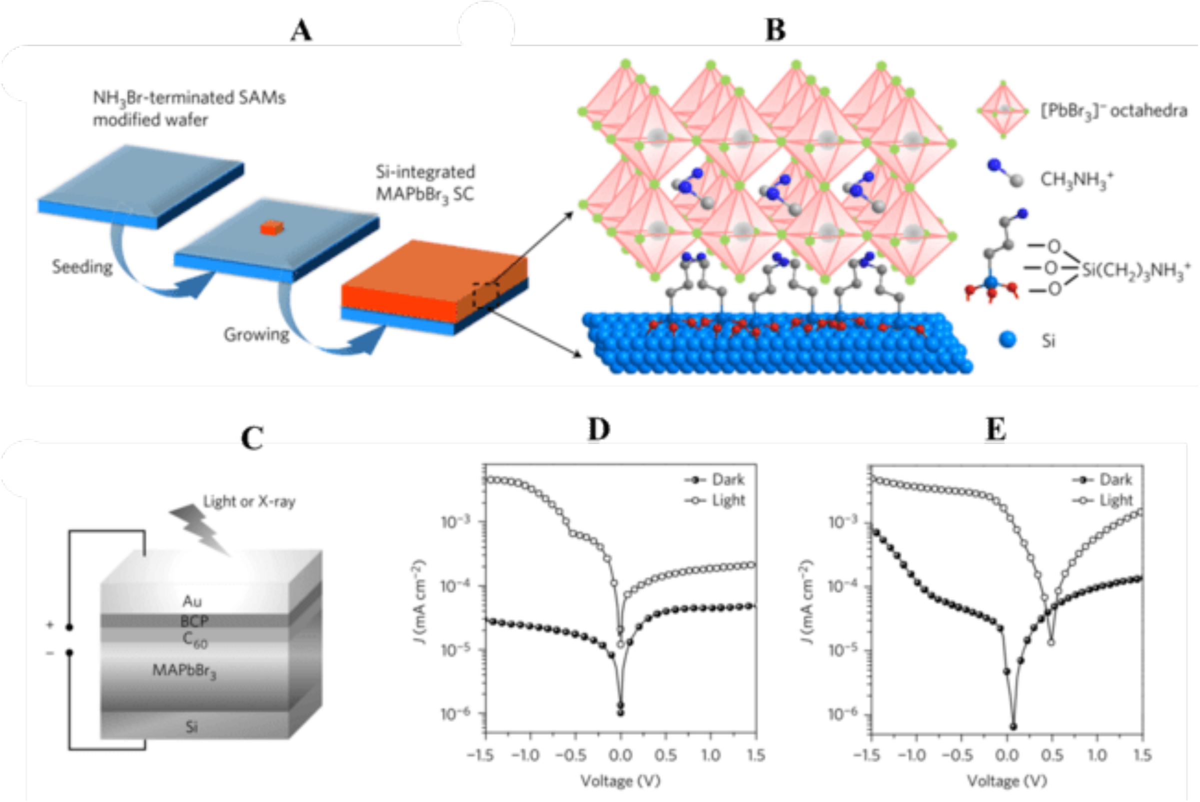

FIGURE 5. SCs of Si-integrated $MAPbBr_3$ and device properties. (A, B) Si-integrated $MAPbBr_3$ SCs attached through APTES. (C) $MAPbBr_3$-based X-ray detector configuration. (D) Dark current and photocurrent density of the Si-integrated $MAPbBr_3$ SC device and (E) $MAPbBr_3$ SC device with Au-anode (control device). Reproduced with permission [25].

Shrestha *et al*. [25] fabricated a $MAPbI_3$ wafer-based photodetector by applying 15 MPa for 2 min using a hydraulic press, and the device showed a remarkable conversion efficiency of 2,527 μC Gy_{air}^{-1} cm^{-2} under 70 kV_p X-ray exposure. Zhao *et al*. [94] developed a new approach for flexible X-ray detectors. They developed a new fabrication method for large-area and flexible perovskite membranes with an area of 400 cm^2 by infiltrating saturated perovskite solution via porous polymer membranes by vacuum pumping, followed by hot lamination. The fabricated X-ray detector reached a sensitivity of 8,696 ± 228 μC Gy_{air}^{-1} cm^{-2}. Recently, Xu *et al*. [95] developed an ultra-flexible sandwich structure thin film scintillation screen synthesized by spin-coating that showed high sensitivity and low-cost, stable X-ray imaging. They obtained a flexible scintillation screen with a three-step process. First, they spin-coated a thin polymer layer onto quartz substrates. Then $MAPbBr_3$ perovskite QDs solution was spin-coated on the polymer surface. Finally, a polymer surface was coated on top of the perovskite layer. Ultimately, the polymer-perovskite QD-polymer (PPP) scintillation screen was peeled off from the substrate for different measurements.

7.2.1 Electronic integration and encapsulation methods

X-ray imaging detectors based on currently available approaches can be classified into direct- and indirect-type X-ray detectors. For direct detection, the electrical contact between perovskites and front-end circuits should be considered and for indirect detection, perovskite scintillators should be coupled with photosensors [92,96]. For indirect-type X-ray detectors, GOS and CsI:Tl materials are commonly used as scintillators [97–99]. Heo *et al.*[92] developed a cost-effective $CsPbBr_3$ NCs scintillator and demonstrated a high-performance indirect-type X-ray detector with high spatial resolution, sensitivity, and stability. The $CsPbBr_3$ NC film was fabricated by spin-coating on a glass substrate and the obtained film was then directly paired CMOS arrays and Si-PDs. The $CsPbBr_3$ NC-based X-ray detector exhibited a higher spatial resolution of 9.8 lp mm^{-1} at modulation transfer function (MTF) = 0.2, a faster response time and comparable stability compared with the commercialized GOS:Tb, based detectors [92]. To protect perovskite scintillators from both mechanical and chemical damages and enhance their stability under ambient conditions, encapsulation is crucial for MHP X-ray detectors. Encapsulation materials should be highly transparent to high-energy X- and γ-rays. Polymer and thin-film encapsulation (TFE) are suitable for traditional radiation detectors [100]. Polyethylene terephthalate (PET), polytetrafluoroethylene (PTFE), poly(methyl methacrylate) (PMMA), etc. are among the commonly used polymers for encapsulation in MHP X-ray detectors. The layer of Al_2O_3 or SiO_2 for encapsulation can be provided by various TFE processes, like chemical vapor deposition (CVD), plasma enhanced chemical vapor deposition (PECVD), physical vapour deposition (PVD), and atomic layer deposition (ALD) [101]. Furthermore, many researchers have also used metal foils for encapsulation: for example, Rocha *et al*. [102] encapsulated CsI:Tl scintillators by aluminum walls. Zhang *et al*. [103] successfully fabricated a highly efficient X-ray detector based on $Cs_2AgBiBr_6$ film encapsulated with a 100-μm-thick Be window. The resulting $Cs_2AgBiBr_6$ device showed efficient X-ray detection with a low dose rate of 145.2 $nGy_{air}\ s^{-1}$ and a detection sensitivity of up to 1.8×104 μC $Gy_{air}^{-1}\ cm^{-2}$.

8. Different dimensional perovskites and their scintillation performance

This section presents a detailed discussion of the different dimensional perovskites and related materials used for radiation detection.

8.1 Organic-inorganic 3D perovskites ($MAPbBr_3$, $MAPbI_3$, $FAPbI_3$)

The 3D ABX_3 perovskite structure is made up of a continuous network of corner-sharing $[BX_6]^{4-}$ octahedra with A-site cations filling in the gaps. Since the light yield of X-ray scintillation is inversely proportional to the optical bandgap, perovskite crystals have many advantages in this application. Low-bandgap perovskites $MAPbI_3$ (1.51 eV) and $MAPbBr_3$ (2.18 eV) have theoretically calculated photon yields of about 270,000 and 190,000 photons MeV^{-1}, respectively, which are higher than the current state-of-the-art cerium (Ce^{3+}) doped lanthanum tribromide $LaBr_3$ ($E_g = 5.90$ eV) [104] and Ce^{3+} doped lutetium iodide LuI_3 ($E_g = 4.15$ eV) scintillators [105], which have light yields of 61,000 and 50,000 photons MeV^{-1}. Birowosuto *et al.* studied the X-ray scintillation properties of $MAPbI_3$ and $MAPbBr_3$ SCs synthesized by the slow evaporation and the ITC methods, respectively [22]. Since charge carriers are trapped and detrapped under high-energy excitation, scintillators often generate delayed luminescence or afterglow. To study the trap states, low-temperature thermoluminescence measurements were performed on these SCs. Both crystals have good consistency, with a low density of shallow traps and no deep trap states, resulting in a substantial reduction in afterglow. At room temperature, the light yields of $MAPbI_3$ and $MAPbBr_3$ are approximately 1,000 photons MeV^{-1}, while at 10 K, they are 296,000 and 152,000 photons MeV^{-1}, respectively [22]. The exciton binding energy of $MAPbBr_3$ and $MAPbI_3$ is in the range of 2–70 meV [106]. In 3D perovskites, loosely bound excitonic states are far more susceptible to thermal quenching than tightly bound excitons in 2D perovskites. Thus, 3D perovskite crystals need to operate at much lower temperatures than 2D crystals to achieve optimum scintillation efficiency. The development of high-performance scintillators that can operate properly at cryogenic temperatures is critical for various practical applications. The efficiency of a scintillator generally degrades as the temperature drops. Because of their excellent stability and optical properties at low temperatures, Mykhaylyk *et al.* demonstrated that $APbBr_3$ SCs are a promising material for radiation detection [107]. For hard radiation, $MAPbI_3$ SCs also had a good spectral response and a low dark current [107]. The optical and electronic properties of HPs can be modulated using doping and compositional engineering. At room temperature, Xu and colleagues published a series of studies on the scintillation properties of $MAPbCl_{3-x}Br_x$ crystals [108–110].

8.2 Organic-inorganic 2D perovskites

2D perovskites have the general formula L_2MX_4 where L is a large monocation (e.g., butylammonium (BA), hexylammonium, phenylethylammonium (PEA)), M is a dication (e.g., Sn^{2+} and Pb^{2+}) and X is a halide ion. An inorganic layer is sandwiched between two large organic spacer layers in 2D perovskites. These perovskites have much better intrinsic stability and resistance to humidity than their 3D counterparts because of their higher formation energy and the hydrophobic nature of organic cations. 2D perovskites have been proposed and researched since the 1990s [111]. However, Asai *et al.* were the first to record the 2.0 MeV proton bombardment of 2D $(C_6H_{13}NH_3)_2PbI_4$ thin-films in 2002 [15]. At room temperature, the decay times of $(C_6H_{13}NH_3)_2PbI_4$ and $(C_3H_7NH_3)_2PbBr_4$ were significantly faster than those of many standard inorganic scintillators. Both 2D crystals, however, had thicknesses of less than 0.3 mm. It is worth noting that when it comes to detecting high-energy radiation, thickness is crucial. Scintillators with substantial area and thickness are needed for use in a γ-ray or fast-neutron detector. To increase the thickness of 2D crystals, Koshimizu *at el.* used aromatic ammonium achieving the thickness more than 1 mm [17]. They synthesized $5\times6\times1$ mm^3 SCs of $(C_6H_5(CH_2)_2NH_3)_2PbBr_4$ that exhibited a light yield of 10,000 photons MeV^{-1}, measured at 662 keV γ-ray energy. However, under pulsed X-ray excitation, its main decay time was 9.4 ns, which is comparable to that of $(C_6H_{13}NH_3)_2PbI_4$. When irradiated with γ-rays or X-rays, the absorbed energy of the inorganic layer is much higher than that of the organic layer, so the scintillation properties of organic–inorganic layered perovskite-type compounds are mainly based on inorganic layer exciton properties. Furthermore, the luminescence of perovskites is dominated by two structural distortions: (i) the Pb-Br-Pb bridging bond linking two adjacent $[PbBr_6]^{2-}$ and (ii) the Br-Pb-Br bond of $[PbBr_6]^{2-}$. These structural distortions in perovskites make them ideal for γ-ray detection. Kawano *et al.* recently published an antisolvent diffusion method for synthesizing large $(C_6H_5(CH_2)_2NH_3)_2PbBr_4$ crystals ($17\times23\times4$ mm^3) that had structural distortions and it showed excellent scintillation properties exhibiting a high light yield of 14,000 photons MeV^{-1} under γ-rays and fast response of 11 ns [112]. To increase the structural distortions and light yield, Horimoto *et al.* introduced F on the benzene ring of $C_6H_5(CH_2)_2NH_3$ at the ortho, meta, and para positions individually and synthesized $[n\text{-}FC_6H_4(CH_2)_2NH_3]_2PbBr_4$ {n-FPhe = $FC_6H_4(CH_2)_2$} (n = 2, 3, 4) crystals [113]. Under γ-ray irradiation, however, the light yield was around 3,300 (2-FPhe), 12,000 (3-FPhe), and 8,300 photons MeV^{-1} (4-FPhe), which was still lower than that of $(C_6H_5(CH_2)_2NH_3)_2PbBr_4$ crystals. Several metal ions (e.g., Sr^{2+}, Ba^{2+}, Mn^{2+}, and Li^{+}) have been incorporated in the inorganic layers to improve the light yield. Akatsuka *et al*. doped Sr^{2+} in $(C_6H_5(CH_2)_2NH_3)_2PbBr_4$ $[(C_6H_5C_2H_4NH_3)_2Pb_{1-x}Sr_xBr_4]$ achieving the scintillation light yields of 19,700 and 18,500 photons MeV^{-1} for x = 0.1 and 0.25 samples [114], respectively which are better than that of pure $(C_6H_5(CH_2)_2NH_3)_2PbBr_4$ crystal [113]. A series of Mn^{2+}-doped L_2PbBr_4 [L = n-BA, n-OA, and stearammonium (STA)] was synthesized to improve the light yield [43]. Dopant Mn^{2+} has two advantages: (i) capturing energy from trap states in perovskites and (ii) removing photon loss as the Mn emission photon energy (2 eV) is lower than that of 2D perovskites (3.1 eV). Water-stable Mn-doped STA_2PbBr_4 exhibited the highest light yield of ~24,000 photons MeV^{-1} among the three Mn-doped 2D perovskites (**Figure 6**). Due to the high hydrophobicity of STA organic cation, Mn^{2+}-doped STA_2PbBr_4 showed excellent stability in water. Generally, 3D perovskites are highly unstable in water [115] which is commonly used as a coolant or reaction moderator in nuclear reactors. In this case, Mn^{2+}-doped STA_2PbBr_4 will be highly beneficial for practical applications.

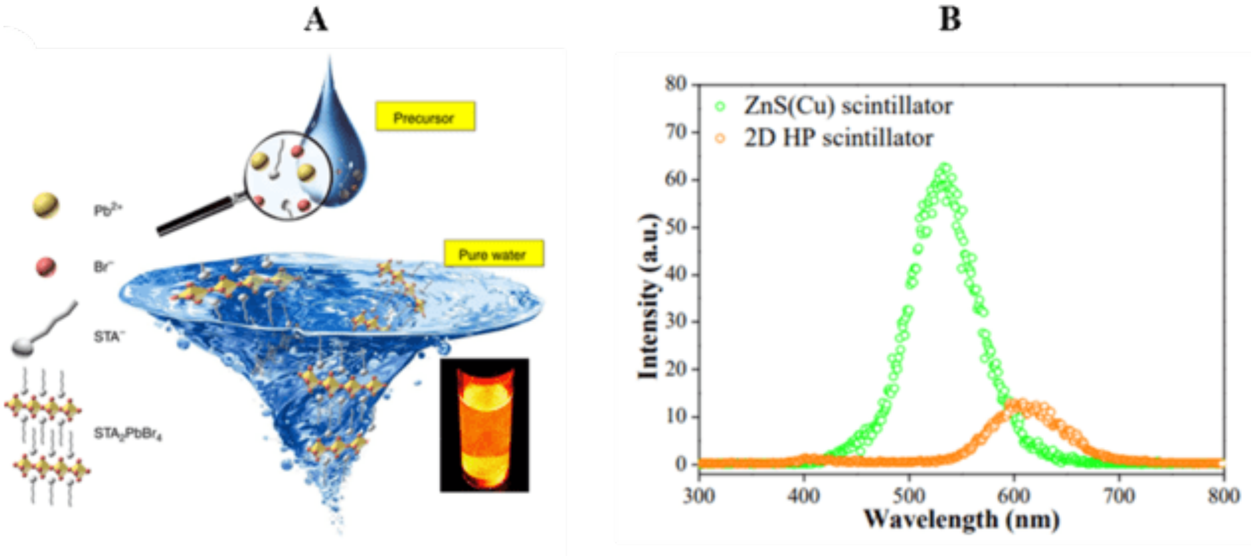

FIGURE 6. (A) Schematic diagram of aqueous synthesis of Mn-doped 2D perovskites. Inset: Mn^{2+}-doped STA_2PbBr_4 under UV light. (B) RL spectra of ZnS(Cu) and Mn^{2+}-doped STA_2PbBr_4 (2D HP). Reproduced with permission.[43]

Alkali metal ions can also enhance the light yield of 2D perovskites. Birowosuto *et al.* doped $(PEA)_2PbBr_4$ with Li-ions. The light yields of undoped and doped crystals were 8,000 ± 800 photons MeV^{-1} and 11,000 ± 500 photons MeV^{-1}, respectively [116]. Later, they found that Li-doping enhanced the light yield of $(PEA)_2PbBr_4$ compared to BA_2PbBr_4 [117]. The Li-doped perovskite crystals showed very fast γ-ray excited scintillation decay, with average decay times of 12.9 ns and 8.0 ns for PEA_2PbBr_4 and BA_2PbBr_4, respectively. The same group also reported a library of 2D HPs and studied their scintillation properties. Among them, BA_2PbBr_4 showed a maximum light yield of 40,000 photons/MeV and rapid decay of 5.3 ns [118]. Although monovalent alkylammonium cation-based 2D perovskites have been studied extensively as scintillators, diammonium cation-based 2D perovskites have rarely been explored. Recently, Birowosuto *et al*. reported $(EDBE)PbCl_4$ 2D perovskite crystals (EDBE = 2,2′-(eth-ylenedioxy)bis(ethylammonium)) with a light yield of 9,000 photons MeV^{-1}, whereas the light yields of 3D $MAPbI_3$ and $MAPbBr_3$ crystals were below 1,000 photons MeV^{-1} [22].

8.3 All-inorganic 3D perovskite ($CsPbBr_3$, $CsPbI_3$)

All-inorganic 3D perovskites have shown promising light yield under high-energy radiation (**Table 4**). Since Voloshinovskii *et al.*'s [119] first observation of the very fast and intense X-ray luminescence of excitons in $CsPbX_3$ (X = Cl, Br, I) at low temperatures in 1993, researchers have been looking into the scintillation properties of all-inorganic halide perovskite SCs. In 2008, Kobayasi *et al.* reported the scintillation properties of $CsPbCl_3$ SCs, which showed a low light yield of ~300 photons MeV^{-1} under γ-ray excitation [120]. At a low temperature (7K), $CsPbBr_3$ SCs exhibited a light yield of 50,000 photons MeV^{-1} under 12 keV X-ray irradiation [121]. Along with SCs, $CsPbX_3$ NCs also show promising scintillation properties. In 2017, Wang Chen *et al.* first explored the scintillation properties of these NCs in different solvents, concentrations, and excitation intensities [122]. Qiushui Chen *et al.* reported the fabrication of multicolor, high-efficiency X-ray scintillators using a series of $CsPbX_3$ NCs [30]. The spin-coated $CsPbBr_3$ nanocrystal film has a low detection limit of 13 nGy s^{-1}, which is around 420 times lower than expected for standard medical diagnostics (5.5 μGy s^{-1}). Under excitation by a ^{137}Cs source (661 keV), this scintillator responds quickly (44.6 ns), suitable for X-ray imaging applications. For this purpose, the authors constructed a simple X-ray imaging system consisting of a $CsPbBr_3$ NC-based background substrate, a digital camera, an α-Si PD array, and a TFT sensor panel, and successfully took an X-ray image of a biological specimen (i.e., a beetle) with a metallic needle.

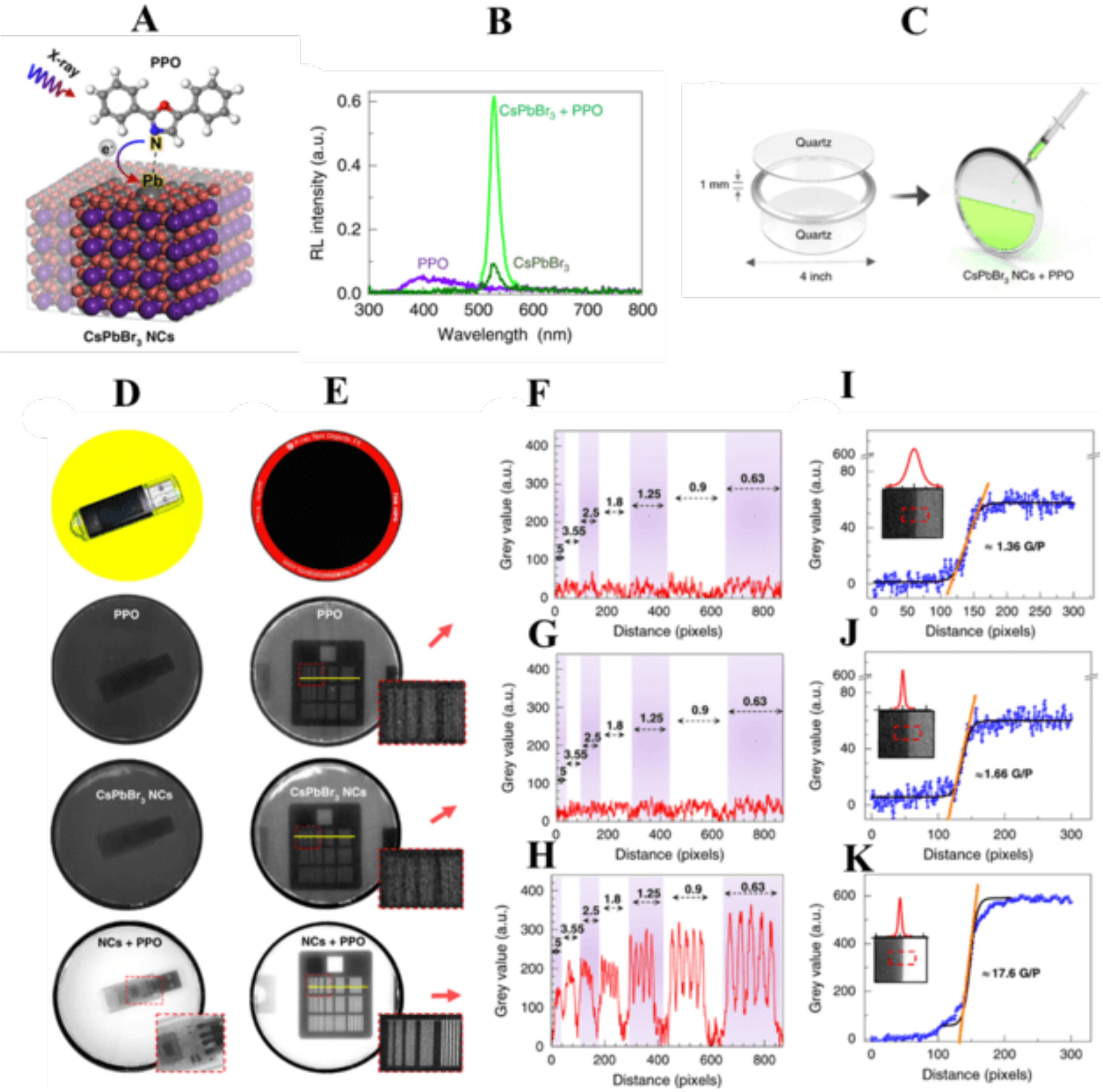

FIGURE 7. CsPbBr$_3$ based liquid scintillator. (A) Schematic diagram showing CsPbBr$_3$ NCs hybridized with PPO. (B) RL spectra of PPO and PPO-CsPbBr$_3$ NCs. The RL intensity of PPO-CsPbBr$_3$ NCs is much higher than those of only PPO and CsPbBr$_3$ NCs. (C) X-ray FPD. PPO-CsPbBr$_3$ NCs dispersed in octane were placed between two quartz windows. (D) Photographs of data storage device on liquid scintillator and X-ray images. (E) Images of the Leeds test objects. (F-H) Line profiles on the line-pair phantom along the yellow lines in Fig. 4E. lp/mm is indicated by numbers (0.63-5). lp/mm: line pair per millimeter. (I-K) Edge spread function (ESF) across

edge of phantom (red box in the inset image). G/P: grey value/pixel. Reproduced with permission [33].

At a spatial resolution of 2.0 lp mm^{-1}, this detector has an MTF value of 0.72, better than that of CsI:Tl-based detector (MTF value of 0.36 at 2.0 lp mm^{-1}). One of the most important features of X-ray image detectors is a large active region, which must be larger than objects such as a patient's body part. On the other hand, spin-coating makes it challenging to make large-area PNC films. Zhang *et al*. described the use of a highly concentrated $CsPbBr_3$ nanosheet by the self-assembly phenomenon for the fabrication of a crack-free thin film with a surface area of 72 cm^2 [123]. Under X-ray illumination, scintillators made from these nanosheets have high RL and long-term stability. Moreover, the light yield of this scintillator film is higher (21,000 photons MeV^{-1}) than that of the commercially available Ce:LuAG single-crystal scintillator (18,000 photons MeV^{-1}). The excellent scintillation output is due to an energy transfer mechanism within the self-assembled $CsPbBr_3$ nanosheets. Cho *et al.* reported a liquid scintillator made up of $CsPbX_3$ (A: Cl, Br, I) NCs hybridized with PPO that can be used for high-resolution X-ray imaging (**Figure 7)** [33]. The hybrid scintillator showed superior spatial resolution with an lp mm^{-1} of at least 3.5, significantly higher than pure HP NCs and PPO scintillators.

Table 4. Scintillation properties of all-inorganic 3D perovskites

Materials	Light yield (photons MeV^{-1})	Decay time (excition source)	Ref.
$CsPbCl_3$ SC	330	0.30, 5.6 ns (X-ray)	[120]
$CsPbCl_3$ SC	~1,200	0.39, 7.0 ns (X-ray)	[124]
$CsPbBr_3$ SC	~50,000 (7 K)	~1 ns (X-ray)	[121]
$CsPbBr_3$ NCs	-	2.87 ns (285 nm)	[92]
$CsPbBr_3$ NCs	-	44.6 ns (^{137}Cs, 661 keV)	[30]

PPO + $CsPbBr_3$ NCs	~ 10 photons keV^{-1}	60−100 ns (γ-ray)	[33]
$CsPbBr_3$ nanosheets	~21,000	1−10 ns (410 nm)	[123]
$CsPbBr_3$@Cs_4PbBr_6 powders	-	3 ns (375 nm)	[125]
$CsPbBr_3$@Cs_4PbBr_6 NCs	64,000	< 10 ns (59.5 keV from ^{241}Am)	[126]
$CsPbBr_3$ NCs@PMMA	~9,000	3.4 - 14.1 ns (400 nm)	[32]

8.4 0D-3D all-inorganic perovskite

The combination of 0D-3D perovskite materials such as $CsPbBr_3$@Cs_4PbBr_6 has been proven to be an effective method for improving scintillation properties. The CsBr bridges completely separate the $[PbBr_6]^{4-}$ octahedrons in the Cs_4PbBr_6 crystal structure, creating 0D perovskite, whereas $[PbBr_6]^{4-}$ octahedrons are connected in all three directions, forming 3D $CsPbBr_3$. While 3D HP NCs are promising, with high scintillation efficiency at room temperature, they are unstable under high-energy irradiation, not only because of their inherent sensitivity to multiple environmental factors such as light, heat, and moisture but also because of well-known aggregation and phase transition issues [126]. As a result, achieving high scintillation efficiency and stable X-ray irradiation performance in HPs is still a difficult task. The "emitter-in-matrix" type material could solve these issues if it has the following properties: (i) the emitter must lead to high-efficiency RL, (ii) the matrix must stop X-rays maintaining high material stability, and (iii) the host must be optically transparent to the emission from the embedded emitter in order to avoid photon loss. For improved stability and performance, Cao *et al.* synthesized a $CsPbBr_3$@Cs_4PbBr_6 "emitter-in-matrix" structure where $CsPbBr_3$ NCs were embedded inside the Cs_4PbBr_6 crystal matrix (**Figure 8**) [125]. The Cs_4PbBr_6 matrix increased X-ray attenuation and the stability of the

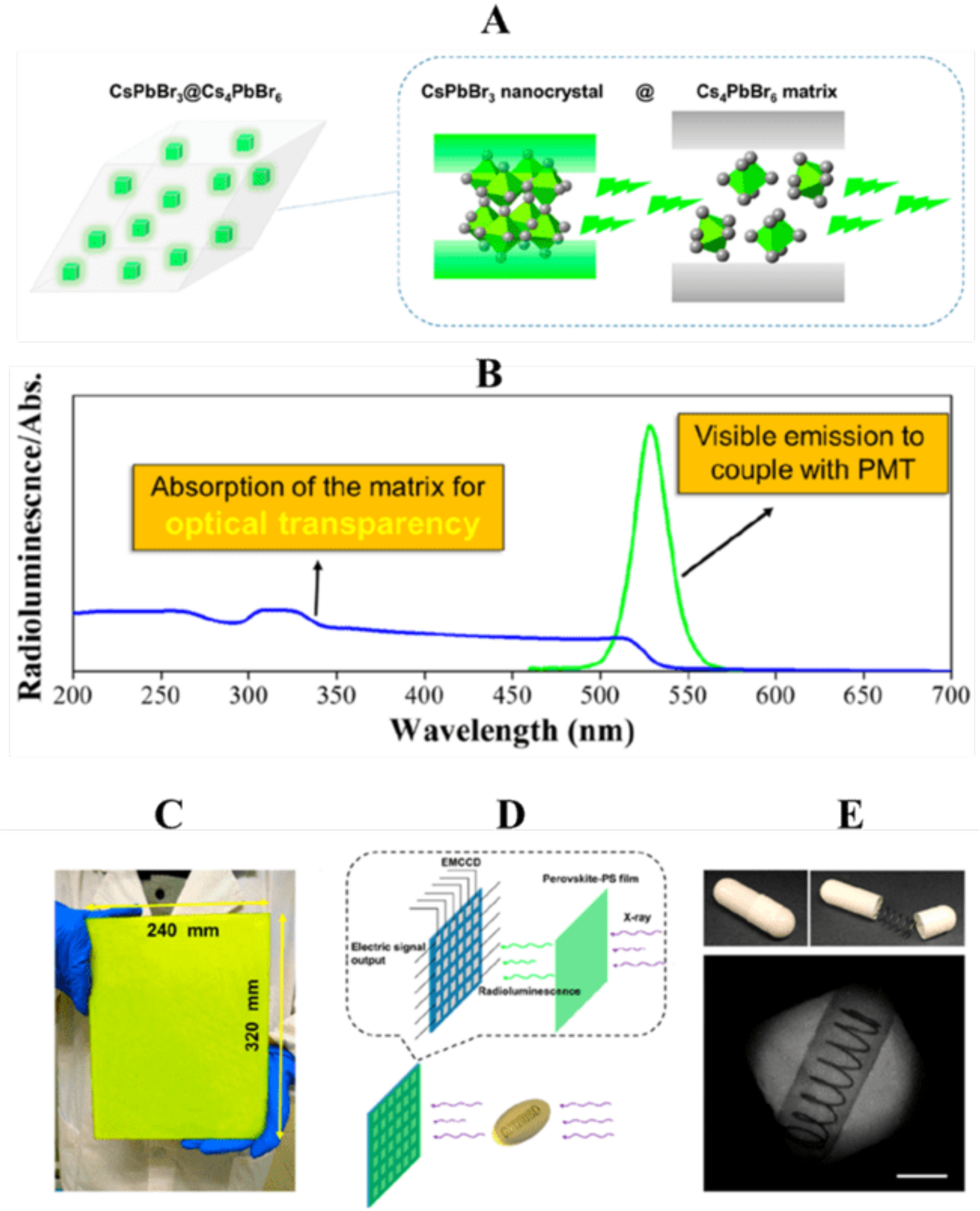

FIGURE 8. (A) $CsPbBr_3@Cs_4PbBr_6$ and schematic diagram of band gap of both 0D and 3D perovskites. The transparent matrix and light emitter were Cs_4PbBr_6 and $CsPbBr_3$, respectively. (B) RL and absorption spectra of $CsPbBr_3@Cs_4PbBr_6$. (C) A low-cost blade-coating process was

used to create a large-area film of $CsPbBr_3@Cs_4PbBr_6$. (D) X-ray imaging set-up. The X-ray source and the sensing component were separated by the target material. The scintillation film was covered on an electron-multiplying CCD to provide the sensing component. (E) Image of a capsule with a metal spring inside and X-ray image using $CsPbBr_3@Cs_4PbBr_6$. The scale bar is 1.5 mm. Reproduced with permission [125].

embedded $CsPbBr_3$ NCs. The wide-band-gap Cs_4PbBr_6 was also transparent to the green emission of $CsPbBr_3$ NCs, minimizing photon loss caused by self-absorption (or photon recycling). As an X-ray projector, a large-area film of $CsPbBr_3@Cs_4PbBr_6$ with a size of 360×240 mm^2 was fabricated, allowing a clear picture of an unseen internal structure to be viewed with high quality, demonstrating its great potential for practical use. Xu *et al.* fabricated a similar composition ($CsPbBr_3/Cs_4PbBr_6$), showing that the $CsPbBr_3/Cs_4PbBr_6$ material possesses excellent radiation hardness and high air stability [126]. The light yield of $CsPbBr_3/Cs_4PbBr_6$ was about 64,000 photons MeV^{-1}, which is around 168% that of NaI:Tl and 156% that of CsI:Na.

8.5 Lead-free 3D double perovskites

While organic-inorganic hybrid lead HPs have shown promise as scintillators, their strong self-absorption, relatively low light yield, and lead toxicity make it necessary to substitute lead and volatile organic counterpart. Hence, nontoxic perovskites with a high scintillation light yield against high-energy radiations are desired. In addition, lead HPs often exhibit ionic migrations under an electrical field, resulting in baseline drift, increased noise, and thus signal difficulty. Indirect radiation detection using metal HPs could eliminate the ionic migration issue. By forming a double perovskite structure $A_2B'B''X_6$, in which A is Cs, B' is a monovalent metal (Ag^+, Na^+, etc.), B'' is a trivalent metal (Bi^{3+}, In^{3+}, etc.), and X is a halide, lead can be replaced with heterovalent metals. Because of their all-inorganic constituents, these materials typically have strong thermal and moisture stability, indicating that they may be used in optoelectronic devices. Using a hydrothermal process, Tang group created lead-free double perovskite crystals based on lanthanides ($Cs_2NaTbCl_6$ and $Cs_2NaEuCl_6$) [127]. The light yield of $Cs_2NaTbCl_6$ under X-ray radiation was 46,600 photons MeV^{-1}, which is substantially higher than that of lead-based HPs.

Reducing the self-absorption effect is the most effective way to improve light yield. The self-absorption effect can be reduced by using double perovskites with a large Stokes change between the radioluminescence (RL) and absorption spectra that gain from self-trapped excitons (STEs). Zhu *et al*. described a series of nontoxic double-perovskite scintillators made of $Cs_2Ag_{0.6}Na_{0.4}In_{1-y}Bi_yCl_6$ in which the X-ray absorption coefficient, radiative emission efficiency, light yield, and light decay were all manipulated by changing the heavy atom Bi^{3+} material (**Figure 9**) [128]. Due to its negligible self-absorption effect, the light yield of $Cs_2Ag_{0.6}Na_{0.4}In_{0.85}Bi_{0.15}Cl_6$ is up to 39,000±7000 photons MeV^{-1}, considerably higher than that of the previously recorded $CsPbBr_3$ NCs (21,000 photons MeV^{-1}).

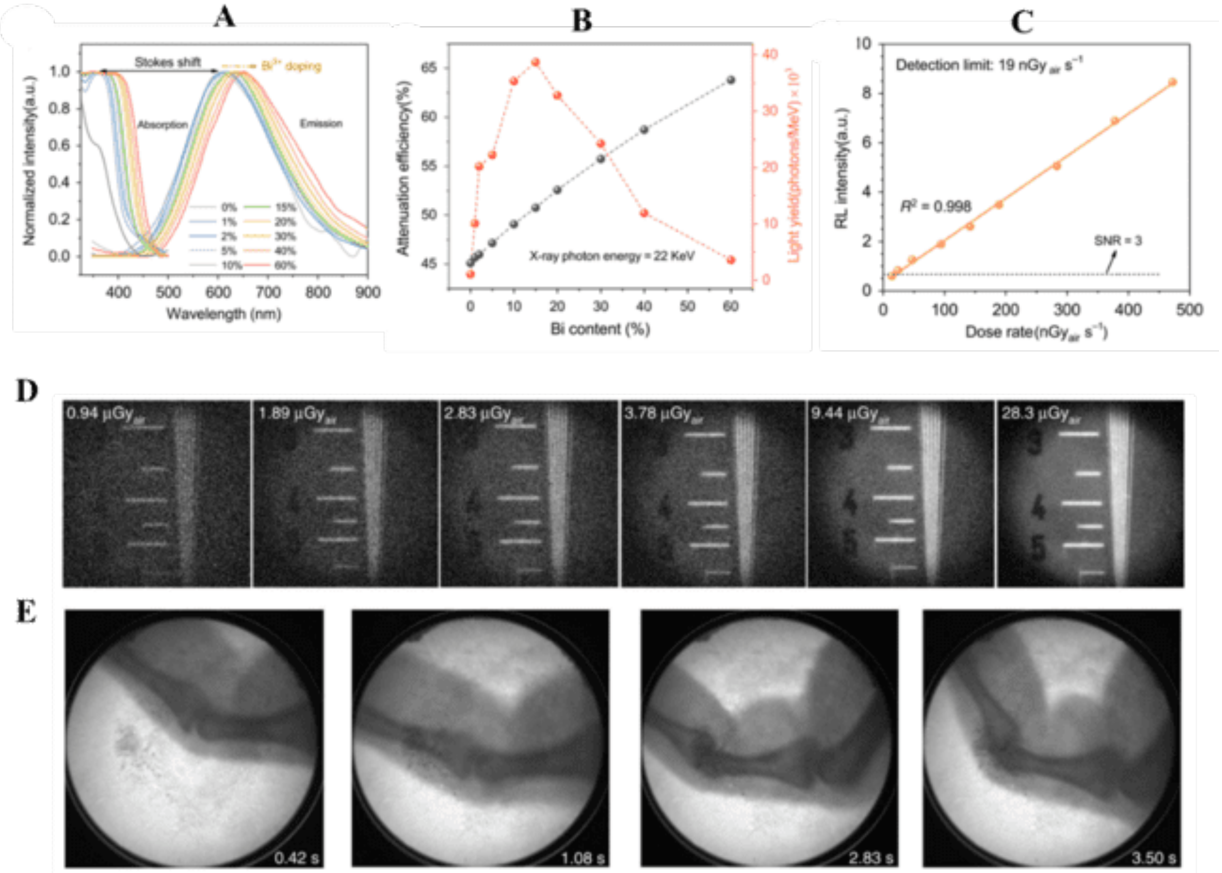

FIGURE 9. (A) Stokes shift of $Cs_2Ag_{0.6}Na_{0.4}In_{0.85}Bi_{0.15}Cl_6$ with different Bi^{3+} concentrations. (B) Attenuation efficiency and light yield of $Cs_2Ag_{0.6}Na_{0.4}In_{0.85}Bi_{0.15}Cl_6$ versus amount of Bi^{3+}. (C) RL intensity as a function of dose rate, revealing detection limit of $Cs_2Ag_{0.6}Na_{0.4}In_{0.85}Bi_{0.15}Cl_6$. (D)

X-ray photographs of test-pattern plate taken at various X-ray doses. (E) Finger bending in real-time X-ray images (dose rate: 47.2 $\mu Gy_{air}\ s^{-1}$, voltage: 50 kV). Reproduced with permission [128].

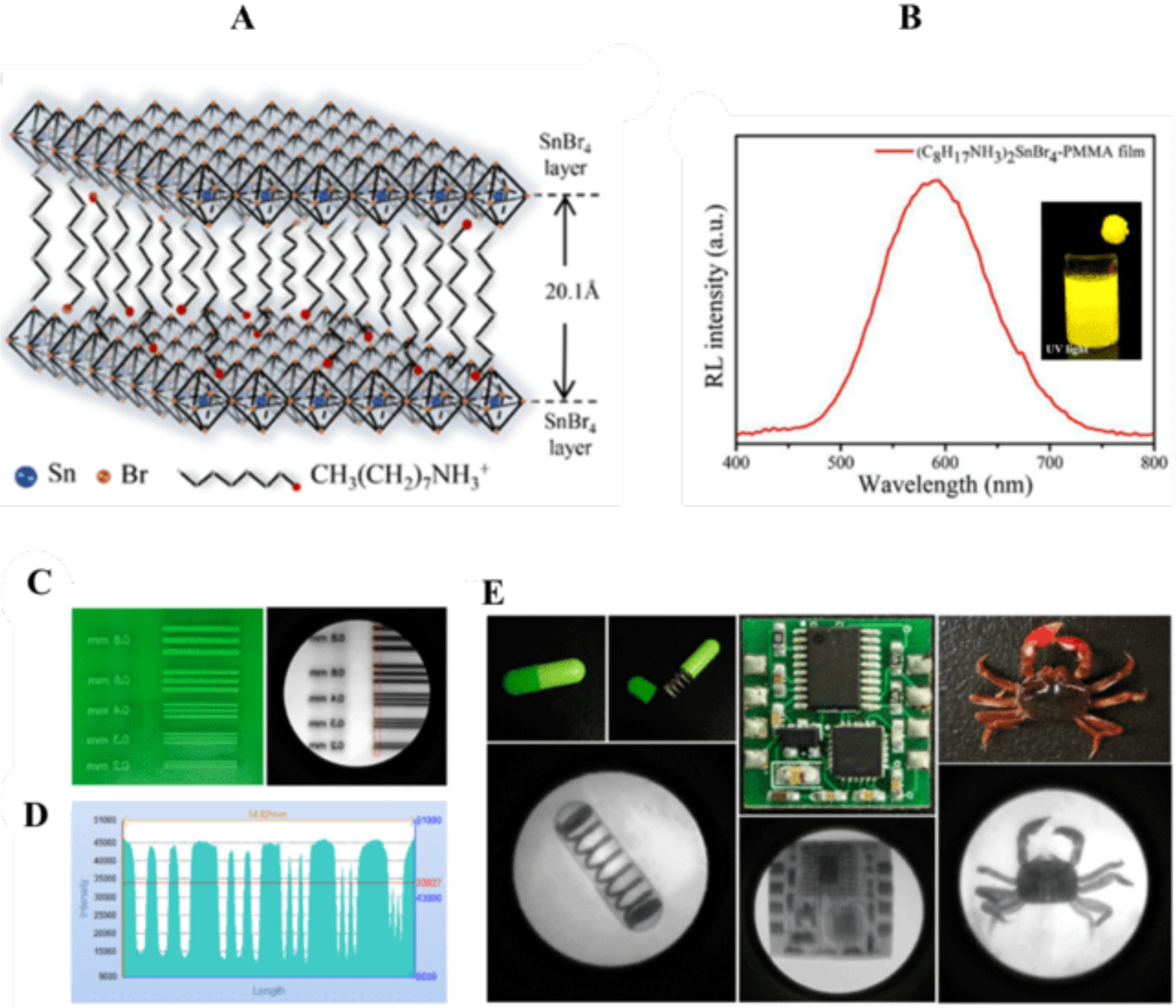

FIGURE 10. Scintillation properties and X-ray imaging of 2D-$(C_8H_{17}NH_3)_2SnBr_4$ perovskite. (A) Schematic diagram of the 2D layered crystal structure of $(C_8H_{17}NH_3)_2SnBr_4$. (B) RL spectrum of a $(C_8H_{17}NH_3)_2SnBr_4$-PMMA film. Inset: image under UV light. (C) Image of target materials. (D) The contour profiles of image (C), (E) Photo and X-ray images of a capsule with a metal spring inside, a circuit board, and a biological specimen (crab). Reproduced with permission [129].

Static X-ray imaging was achieved at a low dose of ~1 μGy$_{air}$, and dynamic X-ray imaging of finger bending without ghosting was shown at a low dose rate of 47.2 μGy$_{air}$ s^{-1}, thanks to this scintillator's high light output and rapid light decay. The RL strength and X-ray image quality remained nearly unchanged after 50 h thermal treatment at 85 °C accompanied by 50 h X-ray irradiation in ambient air. Using Ce ions as a sensitizer in lead-free double-perovskite (DP) crystals could improve X-ray detection and imaging sensitivity by increasing the X-ray stopping power. Ce:$Cs_2NaTbCl_6$ crystals have a light output of 52,153 photons MeV^{-1}, 25% higher than that of undoped crystal, and a detection limit of 30 nGy s^{-1} (roughly 1/183 of a normal medical imaging dose), and the scintillation film has a spatial resolution of up to 10 lp mm^{-1} [130].

8.6 Lead-free 2D perovskites

The development of lead-free 2D perovskites as scintillators is important due to their higher stability as compared to their 3D counterparts. Recently, Gu *et al*. developed a lead-free 2D perovskite ($(C_8H_{17}NH_3)_2SnBr_4$) scintillator [129]. This perovskite showed a PL peak at 596 nm and nearly 100% PLQY with a long-lived luminescence of τ = 3.34 μs. Furthermore, they embedded $(C_8H_{17}NH_3)_2SnBr_4$ in a polymer matrix to fabricate a uniform flexible scintillator film. Using this film, the team captured images with a resolution of 200 μm (**Figure 10**). These findings reveal the potential applications of $(C_8H_{17}NH_3)_2SnBr_4$ as a next-generation scintillator with low cost, nontoxicity, and good resolution.

8.7 Lead-free low dimensional (0D and 1D) metal halides

Low light yield under high-energy radiation and the toxicity of lead HPs severely restrict their practical application. Lead-free low-dimensional all-inorganic and organic-inorganic hybrid metal halides show efficient luminescence and high stability, making them highly attractive for high-energy radiation detectors. 0D metal halides are an important class of light emitter in which anionic metal polyhedrons are separated by organic or inorganic cations and they show highly efficient Stokes-shifted broadband emissions [131]. Kovalenko *et al*. synthesized group 14 metal-based 0D compounds, $Bmpip_2MBr_4$ (Bmpip = 1-butyl-1-methylpiperidinium cation and M = Ge, Sn, Pb). The RL of Sn and Pb halides is comparable to the brightness of an inorganic commercial X-ray scintillator (NaI:Tl) [132]. However, Sn(II) is prone to oxidation, making this scintillator highly unstable, and Pb is highly toxic. Therefore, the development of highly stable organic 0D metal halide hybrids as scintillators with high light yield and stability under X-ray irradiation is of great interest. Ma *et al*. synthesized an organic Sb(III) chloride-based scintillator with a high light yield of 54,000 photons/MeV, a low detection limit of 191.4 $\mathrm{nGy_{air}\ s^{-1}}$, and excellent stability of over 2 years [133]. Recently, they also reported a 0D, inch-sized Mn-based organic-inorganic X-ray scintillator, ethylenebis-triphenylphosphonium manganese (II) bromide ($(C_{38}H_{34}P_2)MnBr_4$) [134]. It exhibited an emission peak at 517 nm with a PL quantum efficiency (PLQE) of 95%. It showed a very high light yield of 80,000 photons $\mathrm{MeV^{-1}}$ and a low detection limit of 72.8 nGy $\mathrm{s^{-1}}$. The scintillation properties of lanthanide-based 0D halides have rarely been investigated. Wu *et al.* reported all-inorganic Cs_4EuX_6 (X=Br, I) SCs as self-activated scintillators with excellent performance under gamma-ray irradiation. Cs_4EuBr_6 and Cs_4EuI_6 showed high light yields of 78,000 ± 4000 photons $\mathrm{MeV^{-1}}$ and 53,000 ± 3000 photons $\mathrm{MeV^{-1}}$ under ^{137}Cs γ-ray irradiation, respectively [135].

Tang *et al.* reported lead-free halide SCs, namely Rb_2CuBr_3 [136], K_2CuBr_3 [137], and Rb_2CuCl_3 [138], as scintillators with exceptionally high light yields. Moreover, 1D Rb_2CuBr_3 showed a violet emission (385 nm) and a high PL QY (98.6%). It exhibited a very high light yield of ≈ 91,056 photons $\mathrm{MeV^{-1}}$ and excellent spectral stability over 2 months under ambient conditions. In the case of 1D K_2CuBr_3, the PL QY is 86.98% for the violet emission (391 nm), and the light yield is 23,806 photons $\mathrm{MeV^{-1}}$ whereas Rb_2CuCl_3 demonstrated a PL peak at 397 nm and light yield of 16,600 photons $\mathrm{MeV^{-1}}$. The excellent scintillation yield, low toxicity, and good stability indicate that alkali metal-based copper halides could be promising X-ray scintillators. Wu *et al.* presented 0D $Cs_3Cu_2I_5$ SCs with a high scintillation yield of 32,000 photons $\mathrm{MeV^{-1}}$ and 29,000 photons $\mathrm{MeV^{-1}}$ under X-rays and γ-rays, respectively. Along with SCs, $Cs_3Cu_2I_5$ NCs are also gaining attention as X-ray scintillators [139]. These NCs showed efficient and reabsorption-free RL with a high light yield of 79,279 photons $\mathrm{MeV^{-1}}$ under X-rays (**Figure 11**) [140].

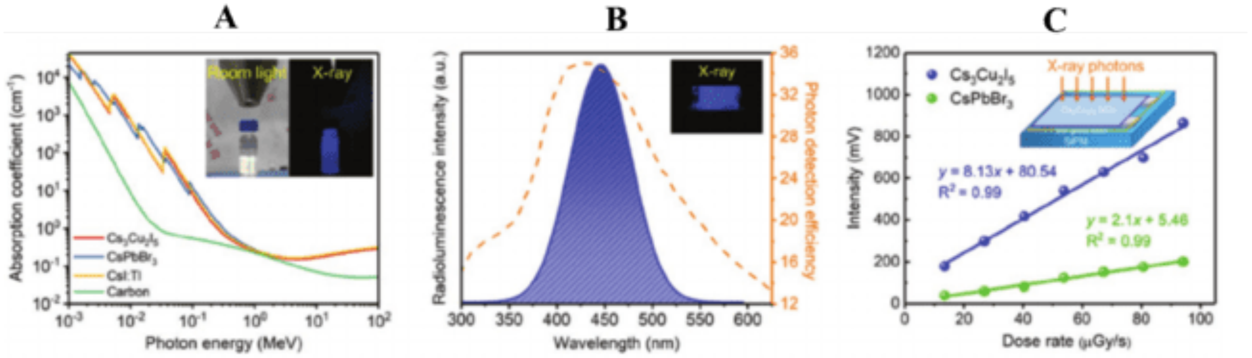

FIGURE 11. (A) X-ray absorption coefficients of $Cs_3Cu_2I_5$, $CsPbBr_3$, CsI:Tl, and carbon dots versus photon energy. Inset: images of colloidal $Cs_3Cu_2I_5$ NCs under room light and X-ray irradiation with a 50 keV. (B) RL spectrum of a NC film and photon detection efficiency. (C) Response intensity of NCs as a function of X-ray dose rate. Reproduced with permission [140].

Wei *et al.* reported a lead-free heterometallic SC, $Cs_4MnBi_2Cl_{12}$, that showed better RL than a commercial NaI(Tl) scintillator [141].

8.8 Polymer encapsulated all-inorganic 3D perovskites

As X-ray scintillators, CsI:Tl and GOS:Tb are now commonly used. The CsI:Tl scintillator requires an expensive and tedious vacuum process to produce a thick crystalline scintillator film, which is inherently brittle and fragile, restricting its use in versatile detection applications like oral and dental imaging. On the other hand, the low-cost and lightweight GOS scintillator is embedded in a flexible matrix. However, it scatters a large portion of the emitted light, lowering the spatial resolution, and has a slow response time, necessitating a long X-ray exposure time to obtain an X-ray image and, as a result, designing a new, cost-effective scintillator with a high spatial resolution and fast response time is highly challenging. Heo *et al.* showed that a low-cost X-ray detector made of a carbon fiber-reinforced polymer film/scintillator film/Si-PD array has high resolution, sensitivity, and stability [92]. They photopolymerized a mixture solution of $CsPbBr_3$ NCs, methylmethacrylate (MMA), and photo-initiator to make the $CsPbBr_3$ NC scintillator film.

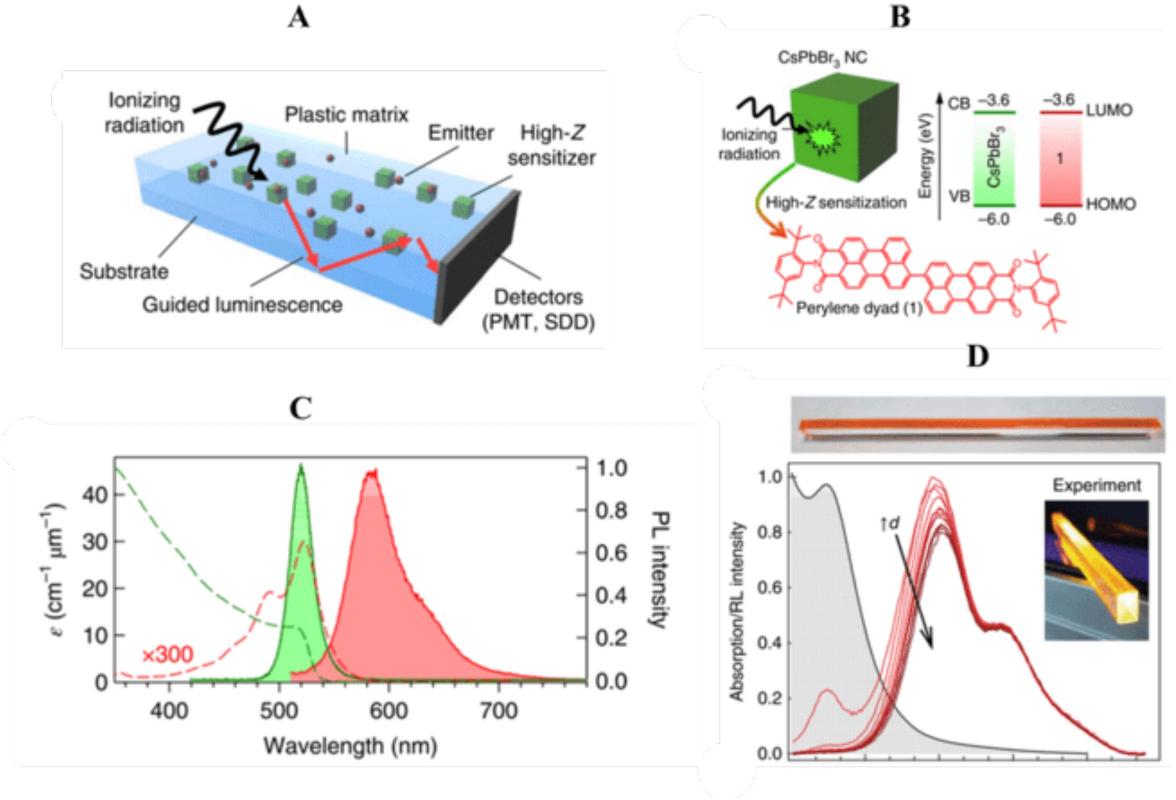

FIGURE 12. Properties of a plastic scintillator made of PMMA nanocomposite embedding CsPbBr$_3$ perovskite NCs. (A) Schematic diagram of the plastic scintillator. (B) Diagram of CsPbBr$_3$ NC sensitizing perylene dyad with an energy band diagram. (C) Absorbance (dashed lines) and PL spectra (solid lines) of NCs (green, excitation wavelength = 405 nm) and perylene dyad, 1 (red, excitation wavelength = 500 nm). (D) Absorption and RL spectra of the plastic scintillator. Photographs of a scintillator waveguide taken under natural light (top panel) and 400 nm UV light (inset in bottom panel). Reproduced with permission [32].

The conversion efficiency of the CsPbBr$_3$ NC film was 45-49%, substantially higher than that of a GOS film (10-24%), and its calculated light yield was 177,000 photons MeV^{-1} (light yield = $10^6/2.5E_g$, where E_g represents the bandgap), higher than 66,000 photons MeV^{-1} for the GOS scintillator. The response time of the CsPbBr$_3$ NCs film (200 ns) was much faster than that of the GOS film (1,200 ns). The authors also contrasted the X-ray images captured by the CsPbBr$_3$ NC and GOS scintillator films. As compared to the commercialized GOS-based detector (spatial resolution = 6.2 lp mm^{-1} at MTF = 0.2 and 6.3 lp mm^{-1} for a linear line chart), the NCs-based X-ray detector had higher spatial resolution (9.8 lp mm^{-1} at MTF = 0.2 and 12.5–8.9 lp mm^{-1} for a linear line chart). Despite significant progress, developing scintillators that effectively combine all of the properties of sensitivity, stability, speed, and loss-free wave-guiding remains a challenge. Reabsorption phenomena reduce the light yield of scintillators. To minimize reabsorption losses in large plastic scintillators, Gandini *et al.* fabricated prototype devices with a PMMA nanocomposite embedding $CsPbBr_3$ NCs as sensitizers for a conjugated organic dye (**Figure 12**) [32]. $CsPbBr_3$ NCs were chosen as high-Z sensitizers because they have a spectrally tunable luminescence, a heavy-metal-based structure, and unparalleled defect tolerance, making them attractive candidates for radiation detection.

9. HPs for high-energy radiation detectors

HPs in various forms, including both polycrystalline and single-crystalline films, have attracted significant attention in the last decade for use in high-energy radiation detectors (**Table 5**) due to exceptional characteristics such as a high absorption coefficient, tuneable bandgap, and high PLQY [37,142,143]. This chapter summarizes various HPs used in high-energy radiation detectors.

9.1 Organic-inorganic 3D perovskites

Large carrier mobility, longer life-time, and smaller trap densities in SC perovskites are essential for long carrier diffusion length, which is crucial for high-energy radiation detectors. In 2015, Huang *et al.* published the first organic-inorganic perovskite radiation detector made of a large $MAPbI_3$ SC (10 mm) with a carrier diffusion length greater than 175 µm. The detector showed photon-to-electron conversion efficiency of 3.9% under γ-irradiation [90]. In the same year, Yakunin *et al*. reported X-ray detectors with photoconductive and photovoltaic (p–i–n junction) architectures using polycrystalline $MAPbI_3$ film [19]. The detector with a photovoltaic architecture had a sensitivity to X-rays of 25 µC mGy_{air}^{-1} cm^{-3}, equivalent to that of α-Se (1-17 µC mGy_{air}^{-1} cm^{-3}). Under X-ray irradiation, a photoconductor with a 60 µm layer of $MAPbI_3$ had a responsivity of 1.9×10^4 carriers/photon. A detector with a high dynamic range and a linear response as a function of intensity is promising for roentgenography, one of the most important uses of X-rays. The $MAPbI_3$ based p–i–n diode has coverage of at least three orders of magnitude, making it ideal for practical use. For efficient X-ray absorption, hybrid HP films with thicknesses of hundreds of micrometers are useful. However, this is difficult to achieve by spin-coating or spray-coating methods. To solve this dilemma, Kim *et al.* successfully grew 830 μm-thick polycrystalline $MAPbI_3$ films and assembled them into photoconductive X-ray detectors using the doctor-blade process [27]. A strong X-ray sensitivity of up to 11 μC mGy_{air}^{-1} cm^{-2} was achieved by combining a broad charge-carrier mobility-lifetime product value of 1.0×10^{-4} cm^2 V^{-1} with high absorptivity and a well-resolved X-ray image was obtained under a low dose of 25 μGy_{air}. Shreetu *et al.* fabricated a rigid, several hundred μm-thick $MAPbI_3$ wafer with a mobility of 0.45–0.7 cm^2 V^{-1} s^{-1} and a μτ product of ~2×10^{-4} cm^2 V^{-1} , nearly three orders of magnitude greater than the polycrystalline $MAPbI_3$ film (2×10^{-7} cm^2 V^{-1}) [25]. At an electric field of 0.2 V μm^{-1}, the detector displayed an excellent conversion sensitivity of 2,527 μC Gy_{air}^{-1} cm^{-2}. Hu *et al.* also fabricated a $MAPbI_3$ wafer-based X-ray detector with a high ambipolar carrier mobility of ~20 cm^2 V^{-1} s^{-1} and a μτ product as high as 3.84×10^{-4} cm^2 V^{-1} [144]. The detector showed a sensitivity as large as 122,000 μC Gy_{air}^{-1} cm^{-2} under a 10 V bias. Due to the imbalanced charge transport properties of electrons and holes, $MAPbI_3$ showed unipolar transport limiting the output in detectors. As a result, improved perovskite materials with higher sensitivity at thickness levels consistent with the requirements of flexible devices and properties such as low operating voltage and balanced ambipolar transport are critical. To accomplish this, Sirringhaus *et al*. used triple cations and synthesized $Cs_{0.05}FA_{0.79}MA_{0.16}Pb(I_{0.8}Br_{0.2})_3$ (TCP), by mixing p-type bromide and n-type iodide constituents [145]. When operated under short-circuit conditions, the resulting thin film devices had a sensitivity of 3.7 μC Gy_{air}^{-1} cm^{-2} to X-rays. When the operating voltage was raised to 0.4 V, it reached a maximum value of 98 μC Gy_{air}^{-1} cm^{-2}.

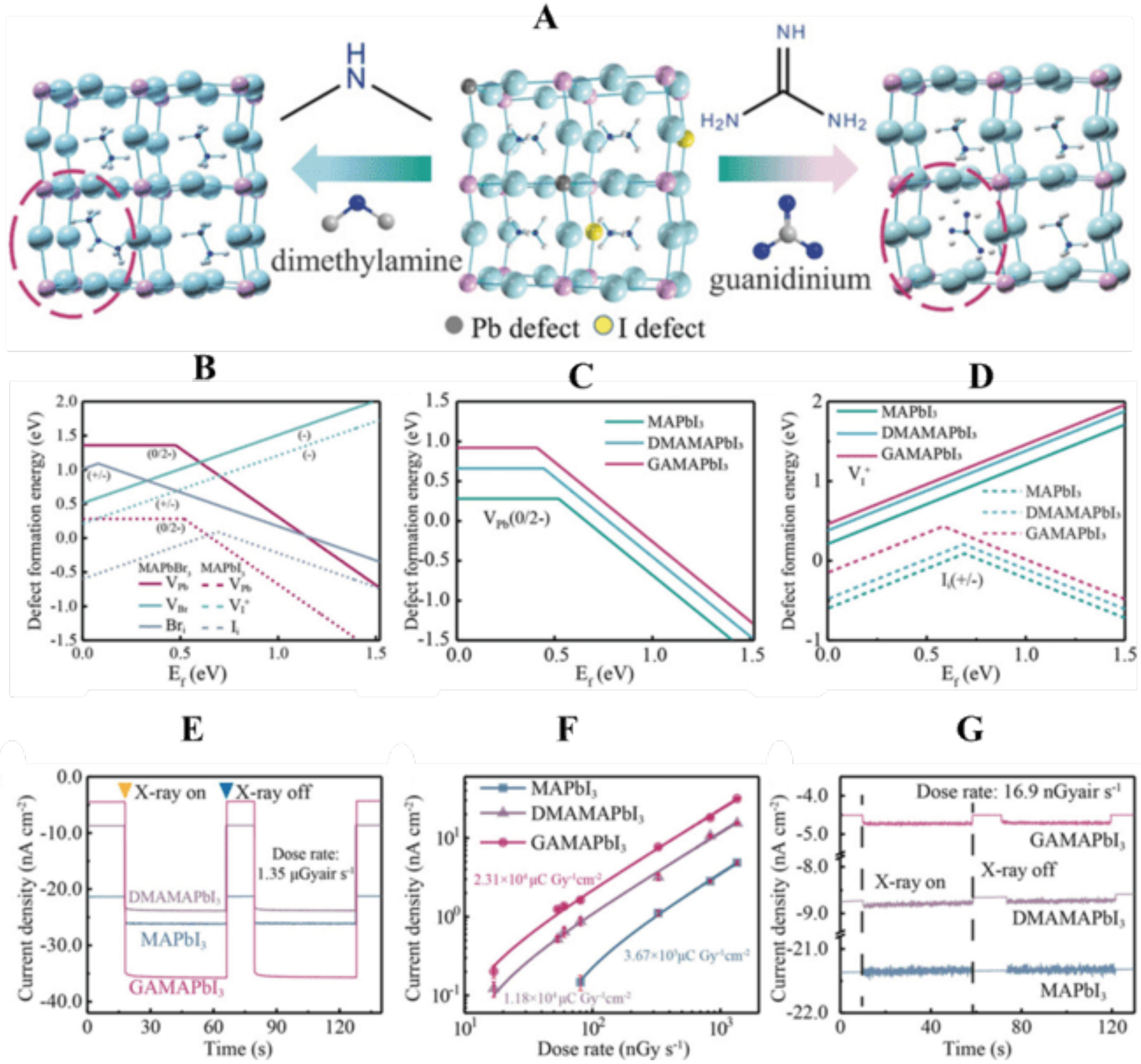

FIGURE 13. (A) Lattice structure and DMA^+ and GA^+ alloying process with $MAPbI_3$. Defect formation energy versus Fermi level E_f of (B) pristine $MAPbBr_3$ and $MAPbI_3$, (C) V_{Pb} for alloyed $MAPbI_3$, (D) V_I and I_i for alloyed $MAPbI_3$. (E) X-ray photo response of X-ray detectors under 1.35 $\mu Gy_{air}\, s^{-1}$ dose rate. (F) Photocurrent versus dose rate of pristine and alloyed X-ray detectors. (G) Photo-switching curves for clean and alloyed detectors at 16.9 $nGy_{air}\, s^{-1}$ dose rate. Reproduced with permission [146].

The sensitivity of TCP was better than that of $MAPbI_3$ (1.5 $\mu C\ Gy_{air}^{-1}\ cm^{-2}$) because of the lower Urbach energy of TCP (14.4 meV) than $MAPbI_3$ (16.7 meV). Urbach energy reduced the degree of disorder, resulting in a higher μτ value. Mescher *et al.* fabricated a triple cation $Cs_{0.1}FA_{0.747}MA_{0.153}PbBr_{0.51}I_{2.49}$ flexible film-based X-ray detector suitable for roll-to-roll fabrication using inkjet printing, allowing them to control its thickness [147]. The detector based on a NiO_x hole transport layer demonstrated excellent stability and sensitivity of 55.4 μC Gy_{air}^{-1} cm^{-2} under a cumulative X-ray exposure of 4 Gy_{air}. This equates to continuous operation for more than 13,000 chest radiographic examinations.

Flexible X-ray detectors are rapidly being developed to realize their huge potential in medicine, engineering, defense, and scientific research. Since they can be bent to fit into non-flat surfaces or view objects in a confined space rather than imaging objects from the outside, where non-targeted sections of the objects filter the X-rays, curved X-ray detectors use less X-rays to provide clearer images than rigid ones. Furthermore, flexible detectors can work with non-uniform X-ray sources in complex applications. Recently, Huang's group reported a large area (400 cm^2) flexible X-ray detector based on $MAPbI_{2.7}Cl_{0.3}$ perovskite-filled nylon membranes [94]. The detector had a μτ product of 1.5×10^{-3} cm^2 V^{-1} and high sensitivity of 8,689 μC Gy_{air}^{-1} cm^{-2}, and it could be bent to radii as small as 2 mm without losing efficiency. Due to the higher atomic number of $MAPbI_3$ ($Z = 49.1$) than $MAPbBr_3$ ($Z = 45.1$), a thinner layer is needed to absorb X-rays completely, and $MAPbI_3$ is expected to outperform $MAPbBr_3$ in terms of X-ray sensitivity. In practice, the efficiency of $MAPbI_3$ in an X-ray detector is still far behind that of $MAPbBr_3$. This is due to electron-photon (e-p) coupling, which speeds up non-radiative relaxation and unstable iodide, which causes iodide vacancies and interstitial defects. Large cations may be alloyed at the A-site to solve the problem. The incorporation of large cations could efficiently reduce the degree of octahedral tilting of the $[PbI_6]^{4-}$ framework, and the strong hydrogen bonds between the organic cations and the inorganic framework would improve the structure's rigidity by suppressing lattice vibration at high frequencies.

Low trap states and weak e-p coupling would increase mobility and suppress nonradiative recombination, allowing efficient charge carrier collection. To increase the efficiency, Huang *et al.* incorporated large cations such as dimethylammonium (DMA^+, 2.72 Å) and (GA^+, 2.74 Å) into $MAPbI_3$ (MA^+, 2.17Å) SCs [146]. In comparison to the pristine $MAPbI_3$ SCs (80.6 nGy_{air} s^{-1}), the novel $GAMAPbI_3$ and $DMAMAPbI_3$ SCs had a lower defect formation energy and lower e-p coupling strength, resulting in a low limit of detection (LOD) of 16.9 nGy_{air} s^{-1} (**Figure 13**). High-quality perovskite SCs with large size are ideal for high-energy detection applications. The high-quality, continuous-mass transport process (CMTP)-grown large SCs of $MAPbI_3$ have higher mobility-lifetime product of 1.6×10^{-3} cm^2 V^{-1}, nearly 450% higher, and lower trap density of 4.5×10^9 cm^{-3}, about 200% lower than the inverse temperature crystallization (ITC)-grown $MAPbI_3$ crystals [148]. The CMTP-grown $MAPbI_3$ X-ray detector's high performance can be compared to that of a high-quality CdZnTe device. $MAPbI_3$ possesses remarkably long electron and hole lifetimes ($\tau_e = 10$ μs and $\tau_h = 17$ μs). The charge collection efficiency (CCE) of electrons and holes in perovskite could affect the detector's performance. As a result, the movement of holes and electrons must be balanced. Kanatzidis *et al.* fabricated a Schottky-type $MAPbI_3$ γ-ray detector that showed a balanced CCE and thereby, a high μτ product ($\sim 0.8 \times 10^{-3}$ cm^2 V^{-1}) was obtained [149]. Despite the fact that the mechanism of X-ray detectors and visible-light photodetectors is the same, a high SNR is required for high sensitivity in the former. Because of its high penetration power, a much thicker active perovskite layer is required to stop X-rays. X-rays are not completely attenuated in thin-film perovskites.

HP SCs possess high mobilities, long carrier lifetimes, and excellent stopping power, and these are ideal for X-ray and gamma-ray detection. Huang *et al*. reported $MAPbBr_3$ SCs with a surface charge recombination velocity of 64 cm s^{-1} and μτ value of 1.2×10^{-2} cm^2 V^{-1} [20]. These properties contributed for developing a detector with a detectable X-ray dose rate of 0.5 μGy$_{air}$ s^{-1} and a sensitivity of 80 μC Gy$_{air}^{-1}$ cm^{-2}. Integration of HP SCs with a Si substrate is an effective method for reducing dark current at higher biases in order to achieve a low X-ray dose and high sensitivity. The mechanical adhesion of $MAPbBr_3$ SCs to Si wafers is very poor due to weak van der Waals interactions. Huang *et al*. integrated a $MAPbBr_3$ SC and Si substrate using brominated APTES [24]. The Si-integrated $MAPbBr_3$ SC detector reveals an extremely low X-ray dose rate of < 0.1 μGy$_{air}$ s^{-1} and a high sensitivity of 2.1×10^4 μC Gy$_{air}^{-1}$ cm^{-2}. Furthermore, the same group reported a dopant compensation strategy in alloyed HP SCs for a better γ-ray detector [26]. Dopant compensation by Cl^- alloying of p-type $MAPbBr_3$ SC significantly reduces the charge carrier concentration while improving the carrier mobility and lifetime, thereby improving CCE. The X-ray sensitivity (to 8 keV X-rays) of the $MAPbBr_{2.94}Cl_{0.06}$ SC detector was 8.4×10^4 μC Gy$_{air}^{-1}$ cm^{-2} with a detection limit of 7.6 nGy$_{air}$ s^{-1}. Yao *et al.* developed a liquid diffused separation induced crystallization method for growing high-quality $MAPbBr_3$ SCs that exhibited a ~ 1 μs lifetime and a low trap density of 4.4×10^9 cm^{-3} [150]. The $MAPbBr_3$ SCs based X-ray detector demonstrated a detectable dose rate lower than 1.2 μGy s^{-1} and a high sensitivity of 184.6 μC Gy^{-1} cm^{-2}. Song *et al.* conducted another interesting study on the facet-orientation-dependent X-ray detection performance of $MAPbBr_3$ SCs [151]. They demonstrated that the [110] $MAPbBr_3$ SC facet has a higher product and SNR than the [100] facet. The [110] facet-based $MAPbBr_3$ X-ray detector outperformed a commercial CsI scintillator in a digital radiography system, with a sensitivity of 3928.3 μC Gy$_{air}^{-1}$ cm^{-2}.

Ohmic and Schottky electrodes are typically formed by combining high and low work function (Φ) metals, respectively, with a p-type semiconductor. With the application of a bias, the large Schottky barrier suppresses ion migration and reduces the leakage current. With a p-type perovskite SC, a larger Schottky barrier is generated at the electrode/perovskite interface with the use of Al than with Au due to the lower work function of Al (Φ_{Al} = 4.28 eV and Φ_{Au} = 5.10 eV). Based on this, Xu *et al.* developed a Schottky barrier at the Al/$MAPbBr_3$ interface by sputtering Al on top of the $MAPbBr_3$ SC, with the resulting barrier significantly reducing the leakage current in a high electric field [152]**.** Consequently, the sensitivity of the detector increased from 62 μC Gy$_{air}^{-1}$ cm^{-2} (Au/$MAPbBr_3$/Au) to 359 μC Gy$_{air}^{-1}$ cm^{-2} (Al/$MAPbBr_3$/Au). Furthermore, the presence of appropriate surface trappings could effectively reduce the interface state density, improving X-ray sensitivity. Li *et al.* used aluminum zinc oxide (AZO) as the surface trapping for fabricating an AZO/$MAPbBr_3$/Au detector, in which the interface state density was dramatically lowered from 2.17×10^{10} to 8.7×10^8 cm^{-2} [153]. As a result, the detector showed an electron mobility lifetime product (μτ) of 2.6×10^{-4} cm^2 V^{-1} and high X-ray sensitivity of ~529 μC Gy$_{air}^{-1}$ cm^{-2}.

Table 5: Characteristic parameters of various direct perovskite detectors

Category	Materials	Characteristic parameters of perovskite detectors				Ref
		μτ product ($cm^2\ V^{-1}$)	Sensitivity ($\mu C\ Gy^{-1}\ cm^{-2}$)	Detection limit ($nGy\ s^{-1}$)	Resistivity (Ω cm)	
Organic-inorganic 3D perovskites	$MAPbI_3$ film	2.0×10^{-7}	-	-	-	[19]
	$MAPbI_3$ wafer	$\sim 2.0 \times 10^{-4}$	2,527	-	-	[25]
	$MAPbI_3$ wafer	3.84×10^{-4}	122,000	-	-	[144]
	$MAPbI_3$ film	1.0×10^{-4}	11,000			[27]
	$MAPbI_3$ SC	3.26×10^{-3}	968.9	-	-	[154]
	$MAPbI_3$ SC	1.6×10^{-3}	-	-	-	[148]
	$MAPbI_3$ SC	-	~700,000	1.5	-	[155]
	$GAMAPbI_3$ SC	1.3×10^{-2}	23,000	16.9	2.05×10^{8}	[156]
	$(3AMPY)Pb_2I_6$ SC	1.2×10^{-4}	207		6×10^{8}	[146]
	$MAPbBr_3$ crystal arrays	-	242	-	-	[157]
	$MAPbBr_3$ SC	4.1×10^{-2}	259.9	-	-	[158]
	$MAPbBr_3$ SC		184.6	<1200		[150]
	$MAPbBr_3$ SC	-	359	-	-	[152]
	$MAPbBr_3$ SC	2.59×10^{-2}	3928.3	<8800	1.25×10^{8}	[151]
	$MAPbBr_3$ SC	2.6×10^{-4}	529	1210	-	[153]
	$MAPbBr_3$ SC	-	23,600	-	-	[159]
	$MAPbBr_3$ SC	-	2,552	-	-	[86]
	$MAPbBr_3$ SC	-	21,000	-	-	[24]
	$MAPbBr_3$ SC	1.2×10^{-2}	80	500	-	[20]
	$MAPbBr_{2.94}Cl_{0.06}$ SC	1.8×10^{-2}	84,000	7.6	3.6×10^{9}	[26]
All-inorganic 3D perovskites	$CsPbBr_3$ film	-	1,450	~500	8.5×10^{9}	[160]
	$CsPbBr_3$ film	-	470	53	-	[161]
	$CsPbBr_3$ film	-	11,840	-	-	[162]
	$CsPbBr_3$ film	1.32×10^{-2}	55,684	215	-	[163]
	$CsPbBr_3$ SC	-	619	-	-	[86]
	$CsPbBr_3$ SC	-	770	-	-	[164]
	$CsPbBr_3$ NC		1,450	-	-	[165]
	$CsPbI_3$ SC	3.63×10^{-3}	2,370	219	7.4×10^{9}	[166]
	$Cs_2AgBiBr_6$ wafer	5.51×10^{-3}	250	95.3	1.6×10^{10}	[93]
	$Cs_2AgBiBr_6$ SC	2.48×10^{-3}	-	-	5.4×10^{9}	[167]
	$Cs_2AgBiBr_6$ SC	-	-	-	3.6×10^{12}	[168]

Double perovskites	$Cs_2AgBiBr_6$ SC	-	316	-	-	[169]
	$Cs_2AgBiBr_6$ SC	6.3×10^{-3}	105	59.7	1.6×10^{11}	[28]
	$Cs_2AgBiBr_6$ SC	5.95×10^{-3}	1,974	45.7	3.31×10^{10}	[170]
	$Cs_2AgBiBr_6$ film	-	18,000	145.2	-	[103]
	$Cs_2AgBiBr_6$/polyvinyl alcohol film		40		2.0×10^{11}	[171]
Low dimensional inorganic perovskites	$Cs_3Bi_2I_9$ SC	7.97×10^{-4}	1652.3	130	2.79×10^{10}	[65]
	$Cs_3Bi_2I_9$ SC	2.03×10^{-5}	111.9	-	1.24×10^{12}	[172]
	$Rb_3Bi_2I_9$ SC	2.51×10^{-3}	159.7	8.32	2.3×10^{11}	[173]
	$(NH_4)_3Bi_2I_9$ SC	1.1×10^{-2}	8,200	210	-	[174]
Low dimensional organic-inorganic perovskites	$MA_3Bi_2I_9$ wafer	4.6×10^{-5}	563	9.3	2.28×10^{11}	[175]
	$MA_3Bi_2I_9$ SC	-	872	31	4.7×10^{10}	[176]
	$MA_3Bi_2I_9$ SC	2.8×10^{-3}	10,620	0.62	5.27×10^{11}	[177]
	$MA_3Bi_2I_9$ SC	2.87×10^{-3}	1,947	83	3.74×10^{10}	[178]
	$(DMEDA)BiI_5$ SC	-	72.5	-	-	[179]
	$(BDA)PbI_4$ SC	4.43×10^{-4}	242	430		[180]
	$(F\text{-}PEA)_2PbI_4$ SC	5.1×10^{-4}	3402	23	1.36×10^{12}	[181]
	$BA_2EA_2Pb_3Br_{10}$ SC	1.0×10^{-2}	6,800	5,500	4.5×10^{10}	[182]
Metal-free perovskite	$DABCO\text{-}NH_4Br_3$ SC	1.2×10^{-3}	173	4960	2.36×10^{8}	[183]

9.2 All-inorganic 3D perovskite

All-inorganic 3D perovskites have improved thermal stability, carrier mobility, and ion migration, suitable for high-energy radiation detectors. However, due to the poor solubility of CsBr in polar solvents, developing high-quality thick $CsPbBr_3$ polycrystalline films is a difficult task. The ability to deposit crack-free thick films effectively is critical for high-energy radiation detection. The rapid and low-cost deposition of hybrids on various substrates makes solution-based processes particularly appealing. Despite the ease of solution processing, potential issues with solubility, surface wetting, and chemical incompatibility between the solvent and hybrid limit their applications. As a result, it is critical to consider alternative film processing techniques. Melt processing is an appealing technique for processing polymeric organic and inorganic materials because it allows for roll-to-roll, lamination, capillary-filling, and extrusion techniques. Mitzi *et al*. developed a melt processing technique to fabricate perovskite films [184].

Recently, several groups have followed the same technique for growing thick perovskite films for high-energy radiation detection. Tang *et al.* fabricated hundreds of micrometers-thick quasi-monocrystalline films of $CsPbBr_3$ with high carrier mobility, a large $\mu\tau$ product, and a photoconductive gain effect [163]. The sensitivity of the as-fabricated $CsPbBr_3$ X-ray detector was 55,684 $\mu C\ Gy_{air}^{-1}\ cm^{-2}$. Matt *et al.* used a similar high-temperature process to melt $CsPbBr_3$ crystals on FTO glass to grow thick $CsPbBr_3$ films [160]. A hotplate was heated to 575 °C to begin the melting process. A variable cooling rate to 560 °C triggered the crystallization of liquid $CsPbBr_3$. The surface exhibited a fine texture at relatively high cooling rates of 0.91 $°C\ min^{-1}$ between 575 and 560 °C, while reducing the cooling rate to $\leqslant 0.25\ °C\ min^{-1}$ expanded the textured areas to cover uniformly wide areas of the substrate. The hole mobility and the resistance of the fabricated $CsPbBr_3$ film were 18 $cm^2\ V^{-1}\ s^{-1}$ and 8.5 GΩ cm, respectively. The sensitivity of the X-ray detector was 1450 $\mu C\ Gy_{air}^{-1}\ cm^{-2}$, comparable to that of cutting-edge Cd(Zn)Te detector technology. Furthermore, a solution-phase dissolution-recrystallization method [161] and a mist deposition method [162] were developed to grow thick $CsPbBr_3$ films. At zero bias and a remarkably low dose rate (0.053 $\mu Gy_{air}\ s^{-1}$), an X-ray photodetector based on solution-phase recrystallized $CsPbBr_3$ microcrystal thick film achieved a sensitivity of 470 $\mu C\ Gy_{air}^{-1}\ cm^{-2}$ [161]. The mist-deposited $CsPbBr_3$ films were up to 110 μm thick, and the $CsPbBr_3$ film-based X-ray detector had a sensitivity of 11,840 $\mu C\ Gy_{air}^{-1}\ cm^{-2}$. NCs of $CsPbBr_3$ have also been used to make X-ray detection films [162,165,185]. Liu *et al.* employed an affordable inkjet printing process to create a large-area homogeneous film of colloidal $CsPbBr_3$ QDs used as an X-ray detector.[165] At a bias voltage of only 0.1 V, this X-ray detector was able to detect a very low X-ray dose rate (17.2 $\mu Gy_{air}\ s^{-1}$) while maintaining a high sensitivity of 1,450 $\mu C\ Gy_{air}^{-1}\ cm^{-2}$.

9.3 3D Double perovskite (DP)

The use of thick perovskite SCs is required in X-ray detectors. A $MAPbBr_3$ SC-based flat-panel X-ray imager with a thickness of 2 mm contains 3,336 g Pb per m^2, far above the European Union Restriction of Hazardous Substances Directive's (EU RoHS) regulatory limit of 1,000 ppm Pb [28]. As perovskites easily degrade in water, any leakage could endanger local biological systems. As a result, lead-free solution-processed SCs-based high-energy radiation detectors with improved sensitivity and detection limits are needed. Lead-free DPs are an excellent alternative as high-energy radiation detectors such as $Cs_2AgBiBr_6$, which replace two hazardous Pb^{2+} in $CsPbBr_3$ with one Ag^+ and one Bi^{3+}. The high atomic number of Ag^+ and Bi^{3+} is suitable for a higher absorption coefficient. It has an average Z value of 53.1, which is greater than $MAPbI_3$ (48.9), $MAPbBr_3$ (45.1), and α-Se (34), allowing for better X-ray attenuation and signal current. In addition, the resistivity of $Cs_2AgBiBr_6$ SCs is higher (10^9–10^{11} Ω cm) than those of $MAPbX_3$ (X = Cl, Br, I; 10^7–10^8 Ω cm). Due to the close correlation between shot noise and dark current, this high resistivity allows for a low dark current and hence a lower noise current. Another interesting feature of this DP is that it exhibits suppressed ion migration. Overall, $Cs_2AgBiBr_6$ SCs for X-ray detection are attractive in reducing toxicity and reaching a low detection limit. For the first time, Tang's team demonstrated an X-ray detector composed of lead-free double-perovskite $Cs_2AgBiBr_6$ SCs (3 mm × 3 mm × 2 mm) manufactured using an ITC method [28]. SCs are superior to thin-films because grain boundaries may be eliminated, resulting in a better μτ product. For high-energy radiation detectors, a high μτ product with a low trap density is always desirable. According to Karunadasa *et al.* the indirect transition characteristic of $Cs_2AgBiBr_6$ ensured a reasonably extended carrier lifetime, implying a good μτ product [186]. Another interesting feature of this DP is that the metal bromide octahedron centers of $Cs_2AgBiBr_6$ are either Bi^{3+} or Ag^+ occupied, and these cations may swap in the lattice, causing DP to lose its perfect symmetry. The Ag^+/Bi^{3+} disorder in the crystal structure was nearly removed using post-annealing and surface treatment, and the μτ value increased from 3.75×10^{-3} cm^2 V^{-1} to 6.3×10^{-3} cm^2 V^{-1}, comparable to that of $MAPbI_3$ (1.0×10^{-2} cm^2 V^{-1}), $MAPbBr_3$ (1.4×10^{-2} cm^2 V^{-1}), and the highest-quality CdZnTe SCs (9.1×10^{-3} cm^2 V^{-1}). The $Cs_2AgBiBr_6$ SCs-based detector demonstrated a minimum detectable dose rate of 59.7 nGy s^{-1} and high sensitivity of 105 μC Gy^{-1} cm^{-2} at room temperature [28]. Temperature significantly affects the performance of radiation detectors. At low temperatures, charge carriers are less vulnerable to electron–phonon scattering, leading to larger drift currents. As a result, the carrier lifetimes of free carriers are very high. Because of the tight low-temperature carrier dispersion, electrons have limited access to a fast recombination pathway right above the CBM. Steele *et al.* found that the sensitivity of a $Cs_2AgBiBr_6$ SC-based detector increased from 316 μC Gy$_{air}^{-1}$ cm^{-2} at room temperature to 988 μC Gy$_{air}^{-1}$ cm^{-2} at liquid-nitrogen temperature [168]. The disorderness of Ag^+/Bi^{3+} ions in DP can also be suppressed by organic cations. Yuan *et al.* introduced PEA organic cation into the $Cs_2AgBiBr_6$ SCs to regulate the order–disorder phase transition. PEA-$Cs_2AgBiBr_6$ SCs based X-ray detector showed high sensitivity of 188 μC $\mathrm{Gy_{air}}^{-1}$ cm^{-2} under a bias of 50 V [187]. Xu *et al.* incorporated another organic cation, BA into the $Cs_2AgBiBr_6$ SCs generating a 2D multilayered DP that showed X-ray sensitivity of 4.2 μC $\mathrm{Gy_{air}}^{-1}$ cm^{-2} [188]. This indicates that there is still a lot of room for improvement in the performance of 2D-DPs.

10. Future applications of perovskite detectors and scintillators

Medical imaging, crystallography, mammography, radiography, airport surveillance, nuclear cameras, CT) particle detectors, gas exploration, and X-ray security are only a few of the most common scintillator applications. Different perovskites were used in various forms (e.g., SCs, thin-films, liquids, and flexible films) for high-energy radiation detection and imaging. The authors anticipate that the applications of perovskites will broaden to include even more fields in the near future.

11. Future challenges and solutions

The fast-growing demand for scintillator devices possessing efficient scintillation, fast emission lifetime, high interaction probability with ionizing radiation, robustness against ionizing radiation, and mitigated reabsorption losses in large-volume/high-density detectors is driven by the need for affordable and reliable ionizing radiation detectors in medical diagnostics, nuclear safety, and fundamental science (e.g., particle physics,). As a result, there is a pressing need to create new non-toxic radiation detector materials that can maximally satisfy all of these standards simultaneously, based on a fundamental understanding of scintillation mechanisms.

12.1 Instability under high-energy radiation and high leakage current

While the stability of perovskites under ambient conditions has been extensively studied and improved, their stability under high-energy radiation needs additional study before commercialization. It may be useful to combine perovskites with conducting polymer and heat-transporting materials such as metal oxides. Ionic migrations occur in lead HPs in the presence of an electrical field generated under high-energy radiation, resulting in baseline drift, increased noise, and therefore signal readout difficulty. The polarization effect caused by ion migration is a major concern when using organic-inorganic hybrid HPs for radiation detection. To prevent any leakage current during operation, the semiconductor film should have a low trap density, low thermal emission (recombination) rate, and good film quality.

12.2 Self-absorption and material defect density in the scintillators

Self-absorption occurs when the scintillator reabsorbs released photons. It is extremely important in determining the scintillator's efficiency. While 3D perovskites usually have a tiny Stokes shift, 0D perovskites have a broad Stokes shift and are much more useful as X-ray scintillators. Enlarging the Stokes shift is an effective method to separate the absorption and emission spectra. CsPbBr3 NCs were used as sensitizers for an organic dye with a broad Stokes shift to create a nearly reabsorption-free plastic scintillator. However, the observed light yield was much lower than that of $CsPbBr_3$ NCs, just 9,000 photons MeV^{-1}. In the future, other types of organic dyes should be tested to increase the light yield. An imperfect SC could affect the light yield by trapping the photo-excited electrons. More investigation on growing high-quality SCs with well-defined morphologies is required.

12.3 Improvement of charge collection efficiency (CCE)

A high-quality Schottky junction in perovskite could be achieved by using electrode materials with different work function (Φ) values, resulting in improved CCE. However, due to a large number of surface defects in a semiconductor, a clean and smooth surface is needed before depositing interface layers to realize a highly rectifying Schottky junction. Surface defects act as carrier traps, pinning the Fermi level at the interface and preventing semiconductors from connecting to different metal layers. HPs are noted for their defect tolerance since these defects trigger energy levels within or near the band edge.

12.4 Hybridization of organic molecules with perovskites

Plastic scintillators, which contain scintillation materials embedded on polymeric matrices, have drawn a great deal of attention because of their light weight, quick response time, low cost, wide-area processing, and high sensitivity for, α-, β-, γ-, and X-rays. Since the interaction probability (P_I) with high-energy radiation is dependent on the effective atomic number of the scintillator, its efficiency can be greatly improved by doping high-Z sensitizers; $P_I \propto Z^n$, where n = 1 to 5 depending on the type of interaction. While significant progress has been made in this area, there is still room for improvement in terms of sensitivity, reliability, and loss-free wave-guiding. An efficient plastic scintillator consisting of 9,9′-bis[perylene-3,4-dicarboxylic-3,4-(*N*-(2,5-di-*tert*-butylphenyl)], PMMA, and a high-Z sensitizer, $CsPbBr_3$ has already been demonstrated, and it is comparable with fast lanthanide scintillators [32]. A variety of perylene dyads, triads, and thermally activated delayed fluorescence (TADF) emitters [189] can be used to boost the performance of plastic scintillators in combination with both aromatic/non-aromatic polymers as plastic matrices and various types of HPs as high-Z sensitizers. High light yield is essential for capturing high-resolution X-ray images. For this purpose, small organic molecules can be hybridized with HPs. PPO hybridized with HP NCs has shown promising results in terms of excellent light yield and high spatial resolution of X-ray images [33].

12.5 X-ray imaging

X-ray imaging is used for various purposes such as security, technology analysis, medical imaging, etc. Generally, the image quality is evaluated using a radiography test phantom-like Leeds test objects. **Figure 14A** shows the resolution test pattern of a Leeds Test Objects TOR 18FG phantom in which different spatial frequencies i.e., line pairs per millimeter (lp/mm) are shown [190]. The imaging performance is evaluated by counting the maximal number of resolvable line pairs per millimeter (lp/mm). **Figure 14B** shows a typical X-ray image of the TOR 18FG taken by a hybrid perovskite scintillator and **Figure 14C** exhibits the gray value intensity profiles along the yellow line in the X-ray image of the line pattern. The largest spatial frequency i.e., detectable lp/mm of this hybrid scintillator was at least 3.5 [33]. If we can increase the spatial frequency, we will be able to get better-quality X-ray images.

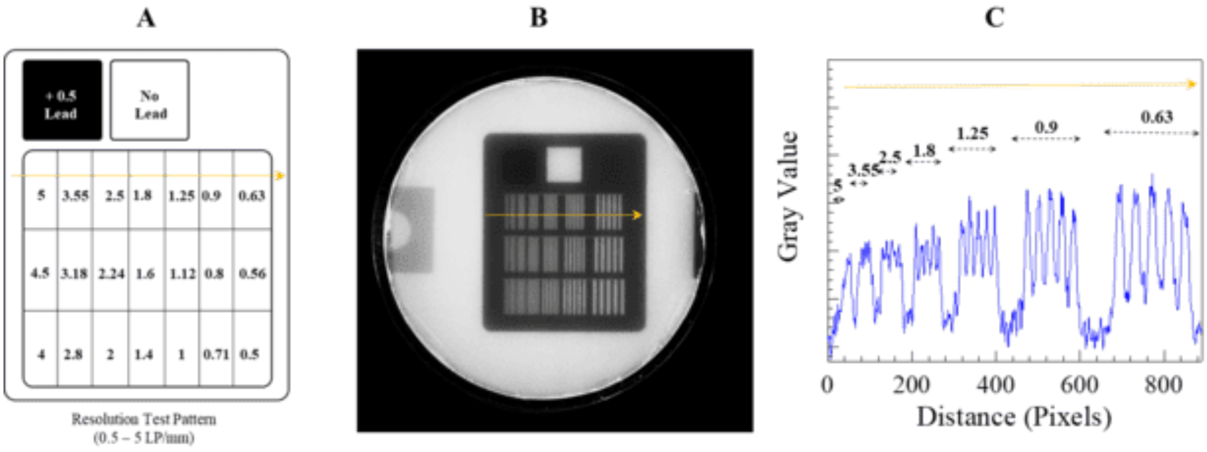

FIGURE 14. X-ray image of the test objects using hybrid perovskite nanocrystals. (A) Schematic of the pattern in the Leeds Test Objects. Numbers (0.5 -5) represent line pairs per millimeter (lp/mm). (B) X-ray image of the Leeds test objects. (C) X-ray line pair profiles along the color line.

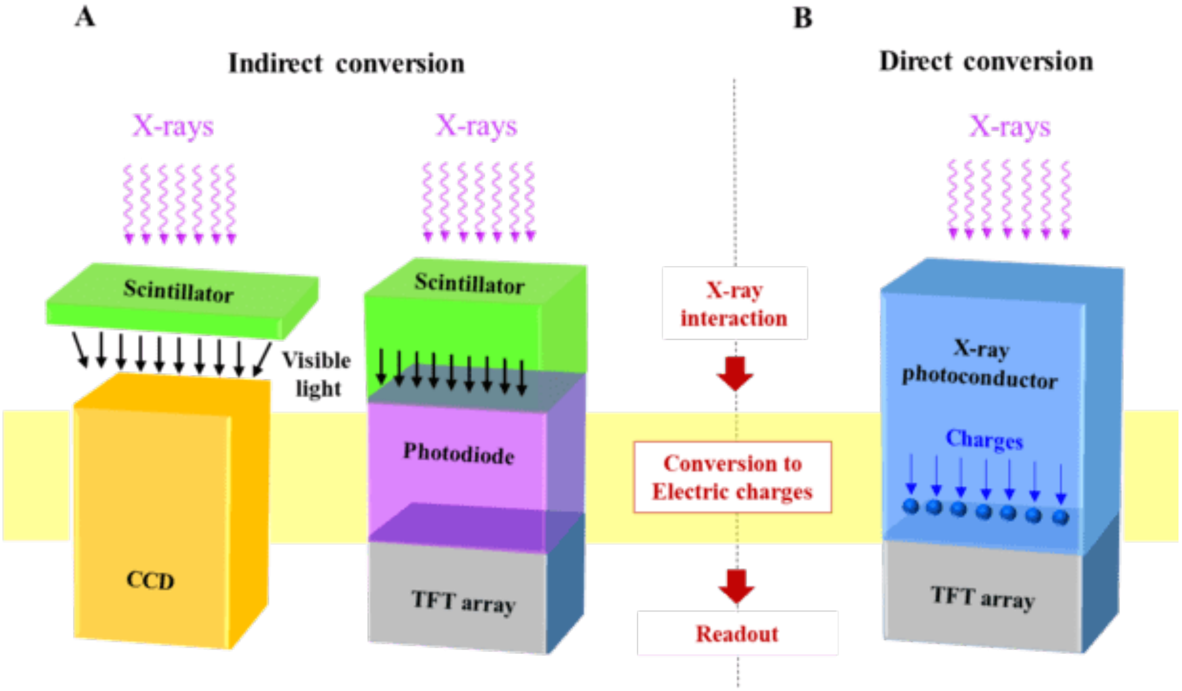

FIGURE 15. Indirect- and direct-readout X-ray detectors. (A) For indirect conversion devices, the scintillator converts X-rays into visible light, which is then converted into an electric charge by the Si photodiode or charge-couple device (CCD). (B) Direct conversion detectors contains an

X-ray photoconductor that transforms X-ray photons directly into electric charges. Thin-film transistor (TFT) arrays can be used in both indirect and direct X-ray detectors.

Indirect conversion flat-panel detectors use a scintillator layer to convert X-ray photons to visible light photons, then converted into an electrical charge using an amorphous silicon photodiode matrix (**Figure 15A**). The quantity and energy of the X-ray photons interact with the detector pixels. Thus, the amount and density of the detector material that absorbs the X-rays determine this charge. Direct X-ray detectors have a higher sensitivity and a lower detection limit than indirect detectors that use scintillators to convert X-rays into visible photons. When X-ray photons collide with a photoconductor, they are transformed directly into electrical signals amplified and digitized in the direct conversion process (**Figure 15B**). Because no scintillator is present, there is no lateral spread of the light photons, resulting in a sharper image. However, the lack of semiconductors that meet the requirements for strong X-ray attenuation, long charge transport properties, and large-area production remains an issue for direct X-ray detectors. Conventional amorphous Se (a-Se) direct X-ray detectors have a very low X-ray attenuation efficiency and a small $\mu\tau$ product (10^{-6} cm^2 V^{-1}), whereas CdZnTe has a high X-ray attenuation efficiency and a high $\mu\tau$ product (10^{-4} cm^2 V^{-1}). However, the large-area fabrication of CdZnTe remains challenging. Recently, lead HPs have been exploited for superior X-ray radiation detection due to their defect-tolerant nature, long carrier lifetime, and low trap density. Furthermore, large-area production of lead HPs is possible using a variety of processes, including screen printing [191], isostatic pressing [192], and melting [193].

12.6 Gigahertz X-ray imaging

Gigahertz (GHz) hard X-ray imaging is essential for future free-electron laser and high-energy physics experiments, such as the nuclear Big Bang and Matter-Radiation Interaction in Extreme (MaRIE) projects [194]. In the MaRIE project, the anticipated X-ray energy and inter-frame time are 30 keV and 2 ns, respectively, in Phase I and 42−126 keV and 300 ps in Phase II. To counteract any pileup effect generated by these high frame rates, non-hygroscopic ultrafast inorganic scintillators with a sub-nanosecond decay duration and high light yields are needed. Current state-of-the-art X-ray imaging technologies operate at about 10 mHz, far below the proposed MaRIE project. Material and structural characteristics impose limitations on both direct and indirect X-ray detection sensors. While direct technology dominates MHz soft X-ray imaging, it has inherent limitations when used in GHz hard X-ray imaging due to the low detection efficiency of the thin detectors necessary for rapid reactions. X-ray imaging cameras with silicon sensors for X-ray detection have achieved a framerate of 10 MHz and outstanding performance for X-ray energy of less than 20 keV. High scintillation photon yields in the initial nanoseconds are achieved using BaF_2 crystals with a sub-nanosecond decay time. This rapid scintillation could be the key to creating an ultrafast front imager. As HP NCs exhibit high scintillation light yields and fast decay times, these NCs may be a promising alternative for GHz hard X-ray imaging.

Acknowledgements

This work was supported by the National Research Foundation (NRF) of Korea (grant nos. 2021R1A2B5B01001796, 2021R1F1A1062672, 2021R1F1A1062528, and 2021R1A4A5031805), and the Technology Innovation Program (grant no. 20013597) funded by the Ministry of Trade, Industry & Energy.

Declaration of Competing Interest

The authors declare that they have no known competing financial interests or personal relationships that could have appeared to influence the work reported in this paper.

Keywords

Perovskite; Scintillator; Direct detector; High-energy radiation; X-ray imaging

References

[1] G.F. Knoll, Radiation Detection and Measurement;John Wiley & Sons: New York, 2010.

[2] G. Blasse, Chem. Mater. 6 (1994) 1465–1475.

[3] N. Zaitseva, A. Glenn, L. Carman, H. Paul Martinez, R. Hatarik, H. Klapper, S. Payne, Nucl. Instrum. Methods Phys. Res. A 789 (2015) 8–15.

[4] N. Balamurugan, A. Arulchakkaravarthi, P. Ramasamy, Nucl. Instrum. Methods Phys. Res. A 568 (2006) 767–771.

[5] A. Lim, G. Hernandez, J. Latta, H.A. Yemam, W. Senevirathna, U. Greife, A. Sellinger, ACS Appl. Polym. Mater. 1 (2019) 1420–1429.

[6] A. Howansky, A. Mishchenko, A.R. Lubinsky, W. Zhao, Med. Phys. 46 (2019) 4857–4868.

[7] K. Saito, S. Sasaki, H. Tawara, T. Sanami, E. Shibamura, Nucl. Instrum. Methods Phys. Res. A 581 (2007) 119–122.

[8] C.H. Lee, J. Son, T.-H. Kim, Y.K. Kim, Nucl. Eng. Technol. 49 (2017) 592–597.

[9] Y. Su, W. Ma, Y. Yang, J. Semicond. 41 (2020) 051204.

[10] R.T. Williams, W.W. Wolszczak, X. Yan, D.L. Carroll, ACS Nano 14 (2020) 5161–5169.

[11] W. Pan, H. Wei, B. Yang, Front. Chem. 8 (2020) 268.

[12] M. Kodur, R.E. Kumar, Y. Luo, D.N. Cakan, X. Li, M. Stuckelberger, D.P. Fenning, Adv. Energy Mater. 10 (2020) 1903170.

[13] M. Sytnyk, S. Deumel, S.F. Tedde, G.J. Matt, W. Heiss, Appl. Phys. Lett. 115 (2019) 190501.

[14] A.N. Belsky, P. Chevallier, P. Dhez, P. Martin, C. Pédrini, A.N. Vasil'ev, Nucl. Instrum. Methods Phys. Res. A 361 (1995) 384–387.

[15] K. Shibuya, M. Koshimizu, Y. Takeoka, K. Asai, Nucl. Instrum. Methods Phys. Res. B 194 (2002) 207–212.

[16] K. Shibuya, M. Koshimizu, K. Asai, H. Shibata, Appl. Phys. Lett. 84 (2004) 4370–4372.

[17] C.W.E. van Eijk, J.T.M. de Haas, P.A. Rodnyi, I. V. Khodyuk, K. Shibuya, F. Nishikido, M. Koshimizu, IEEE Nucl. Sci. Symp. Conf. Rec. (2008) 3525.

[18] C.C. Stoumpos, C.D. Malliakas, J.A. Peters, Z. Liu, M. Sebastian, J. Im, T.C. Chasapis, A.C. Wibowo, D.Y. Chung, A.J. Freeman, B.W. Wessels, M.G. Kanatzidis, Cryst. Growth Des. 13 (2013) 2722–2727.

[19] S. Yakunin, M. Sytnyk, D. Kriegner, S. Shrestha, M. Richter, G.J. Matt, H. Azimi, C.J. Brabec, J. Stangl, M. V. Kovalenko, W. Heiss, Nat. Photonics 9 (2015) 444–449.

[20] H. Wei, Y. Fang, P. Mulligan, W. Chuirazzi, H.-H. Fang, C. Wang, B.R. Ecker, Y. Gao, M.A. Loi, L. Cao, J. Huang, Nat. Photonics 10 (2016) 333–339.

[21] S. Yakunin, D.N. Dirin, Y. Shynkarenko, V. Morad, I. Cherniukh, O. Nazarenko, D. Kreil, T. Nauser, M. V. Kovalenko, Nat. Photonics 10 (2016) 585–589.

[22] M.D. Birowosuto, D. Cortecchia, W. Drozdowski, K. Brylew, W. Lachmanski, A. Bruno, C. Soci, Sci. Rep. 6 (2016) 37254.

[23] O. Nazarenko, S. Yakunin, V. Morad, I. Cherniukh, M. V. Kovalenko, NPG Asia Mater. 9 (2017) e373.

[24] W. Wei, Y. Zhang, Q. Xu, H. Wei, Y. Fang, Q. Wang, Y. Deng, T. Li, A. Gruverman, L. Cao, J. Huang, Nat. Photonics 11 (2017) 315–321.

[25] S. Shrestha, R. Fischer, G.J. Matt, P. Feldner, T. Michel, A. Osvet, I. Levchuk, B. Merle, S. Golkar, H. Chen, S.F. Tedde, O. Schmidt, R. Hock, M. Rührig, M. Göken, W. Heiss, G. Anton, C.J. Brabec, Nat. Photonics 11 (2017) 436–440.

[26] H. Wei, D. DeSantis, W. Wei, Y. Deng, D. Guo, T.J. Savenije, L. Cao, J. Huang, Nat. Mater. 16 (2017) 826–833.

[27] Y.C. Kim, K.H. Kim, D.-Y. Son, D.-N. Jeong, J.-Y. Seo, Y.S. Choi, I.T. Han, S.Y. Lee, N.-G. Park, Nature 550 (2017) 87–91.

[28] W. Pan, H. Wu, J. Luo, Z. Deng, C. Ge, C. Chen, X. Jiang, W.-J. Yin, G. Niu, L. Zhu, L.

Yin, Y. Zhou, Q. Xie, X. Ke, M. Sui, J. Tang, Nat. Photonics 11 (2017) 726–732.

[29] Y. He, L. Matei, H.J. Jung, K.M. McCall, M. Chen, C.C. Stoumpos, Z. Liu, J.A. Peters, D.Y. Chung, B.W. Wessels, M.R. Wasielewski, V.P. Dravid, A. Burger, M.G. Kanatzidis, Nat. Commun. 9 (2018) 1609.

[30] Q. Chen, J. Wu, X. Ou, B. Huang, J. Almutlaq, A.A. Zhumekenov, X. Guan, S. Han, L. Liang, Z. Yi, J. Li, X. Xie, Y. Wang, Y. Li, D. Fan, D.B.L. Teh, A.H. All, O.F. Mohammed, O.M. Bakr, T. Wu, M. Bettinelli, H. Yang, W. Huang, X. Liu, Nature 561 (2018) 88–93.

[31] B. Yang, L. Yin, G. Niu, J.-H. Yuan, K.-H. Xue, Z. Tan, X.-S. Miao, M. Niu, X. Du, H. Song, E. Lifshitz, J. Tang, Adv. Mater. 31 (2019) 1904711.

[32] M. Gandini, I. Villa, M. Beretta, C. Gotti, M. Imran, F. Carulli, E. Fantuzzi, M. Sassi, M. Zaffalon, C. Brofferio, L. Manna, L. Beverina, A. Vedda, M. Fasoli, L. Gironi, S. Brovelli, Nat. Nanotechnol. 15 (2020) 462–468.

[33] S. Cho, S. Kim, J. Kim, Y. Jo, I. Ryu, S. Hong, J.-J. Lee, S. Cha, E.B. Nam, S.U. Lee, S.K. Noh, H. Kim, J. Kwak, H. Im, Light Sci. Appl. 9 (2020) 156.

[34] H. Wu, Y. Ge, G. Niu, J. Tang, Matter 4 (2021) 144–163.

[35] Y. Zhou, J. Chen, O.M. Bakr, O.F. Mohammed, ACS Energy Lett. 6 (2021) 739–768.

[36] H. Wei, J. Huang, Nat. Commun. 10 (2019) 1066.

[37] X. Xu, W. Qian, S. Xiao, J. Wang, S. Zheng, S. Yang, EcoMat 2 (2020) e12064.

[38] Z. Li, F. Zhou, H. Yao, Z. Ci, Z. Yang, Z. Jin, Mater. Today 48 (2021) 155–175.

[39] F. Zhou, Z. Li, W. Lan, Q. Wang, L. Ding, Z. Jin, Small Methods 4 (2020) 2000506.

[40] M.R. Kundu, S.M. White, N. Gopalswamy, J. Lim, Astrophys. J. Suppl. Ser. 90 (1994) 599–610.

[41] Q. Xu, H. Wei, W. Wei, W. Chuirazzi, D. DeSantis, J. Huang, L. Cao, Nucl. Instrum. Methods Phys. Res. A 848 (2017) 106–108.

[42] Y. Ifergan, S. Dadon, A. Ocherashvili, I. Israelashvili, Y. Yehuda-Zada, D. Smadja, L. Carmel, Y. Knafo, D. Ginzburg, A. Osovizky, R. Atias, Y. Kadmon, Y. Cohen, T. Mazor, IEEE Trans. Nucl. Sci. 63 (2016) 634–638.

[43] D. Yu, P. Wang, F. Cao, Y. Gu, J. Liu, Z. Han, B. Huang, Y. Zou, X. Xu, H. Zeng, Nat. Commun. 11 (2020) 3395.

[44] P.A. Rodnyi, P. Dorenbos, C.W.E. van Eijk, Phys. Status Solidi (B) 187 (1995) 15–29.

[45] A. Lempicki, J. Appl. Spectrosc. 62 (1995) 787–802.

[46] M. Moszynski, M. Kapusta, M. Mayhugh, D. Wolski, S.O. Flyckt, IEEE Trans. Nucl. Sci. 44 (1997) 1052–1061.

[47] E. Auffray, G. Dosovitskiy, A. Fedorov, I. Guz, M. Korjik, N. Kratochwill, M. Lucchini, S. Nargelas, D. Kozlov, V. Mechinsky, P. Orsich, O. Sidletskiy, G. Tamulaitis, A. Vaitkevičius, Radiat. Phys. Chem. 164 (2019) 108365.

[48] J.D. Valentine, D.K. Wehe, G.F. Knoll, C.E. Moss, IEEE Trans. Nucl. Sci. 40 (1993) 1267.

[49] J.D. Valentine, W.W. Moses, S.E. Derenzo, D.K. Wehe, G.F. Knoll, Nucl. Instrum. Methods Phys. Res. A 325 (1993) 147–157.

[50] M. Kobayashi, M. Ishii, Y. Usuki, H. Yahagi, Nucl. Instrum. Methods Phys. Res. A 349 (1994) 407–411.

[51] D.R. Kinloch, W. Novak, P. Raby, I. Toepke, IEEE Trans. Nucl. Sci. 41 (1994) 752–754.

[52] T. Fazzini, P.G. Bizzeti, P.R. Maurenzig, C. Stramaccioni, F.A. Danevich, V. V. Kobychev, V.I. Tretyak, Y.G. Zdesenko, Nucl. Instrum. Methods Phys. Res. A 410 (1998) 213–219.

[53] A. Iltis, M.R. Mayhugh, P. Menge, C.M. Rozsa, O. Selles, V. Solovyev, Nucl. Instrum. Methods Phys. Res. A 563 (2006) 359–363.

[54] F.G.A. Quarati, P. Dorenbos, J. van der Biezen, A. Owens, M. Selle, L. Parthier, P. Schotanus, Nucl. Instrum. Methods Phys. Res. A 729 (2013) 596–604.

[55] M. Moszyhski, M. Kapustab, D. Wolski, W. Klamra, B. Cederwall, Nucl. Instrum. Methods Phys. Res. A 404 (1998) 157.

[56] X. Ouyang, B. Liu, X. Xiang, L. Chen, M. Xu, X. Song, J. Ruan, J. Liu, C. Chen, Z. Zhu, Y. Li, Nucl. Instrum. Methods Phys. Res. A 969 (2020) 164007.

[57] N.J. Cherepy, G. Hull, A.D. Drobshoff, S.A. Payne, E. van Loef, C.M. Wilson, K.S. Shah, U.N. Roy, A. Burger, L.A. Boatner, W.-S. Choong, W.W. Moses, Appl. Phys. Lett. 92 (2008) 083508.

[58] J.B. Birks, The Theory and Practice of Scintillation Counting, Elsevier, 1964.

[59] P. Dorenbos, IEEE Trans. Nucl. Sci. 57 (2010) 1162–1167.

[60] P. Dorenbos, J.T.D. de Haas, C.W.V. van Eijk, IEEE Trans. Nucl. Sci. 42 (1995) 2190–2202.

[61] C.A. Klein, J. Appl. Phys. 39 (1968) 2029–2038.

[62] H. Tsai, F. Liu, S. Shrestha, K. Fernando, S. Tretiak, B. Scott, D.T. Vo, J. Strzalka, W. Nie, Sci. Adv. 6 (2020) eaay0815.

[63] H. Mescher, E. Hamann, U. Lemmer, Sci. Rep. 9 (2019) 5231.

[64] S.O. Kasap, J. Phys. D. Appl. Phys. 33 (2000) 2853–2865.

[65] Y. Zhang, Y. Liu, Z. Xu, H. Ye, Z. Yang, J. You, M. Liu, Y. He, M.G. Kanatzidis, S. Liu, Nat. Commun. 11 (2020) 2304.

[66] S.N. Ahmed, Physics and Engineering of Radiation Detection, Elsevier, 2015.

[67] H. Li, C.D. Malliakas, J.A. Peters, Z. Liu, J. Im, H. Jin, C.D. Morris, L.D. Zhao, B.W. Wessels, A.J. Freeman, M.G. Kanatzidis, Chem. Mater. 25 (2013) 2089–2099.

[68] H. Li, C.D. Malliakas, F. Han, D.Y. Chung, M.G. Kanatzidis, Chem. Mater. 27 (2015) 5417–5424.

[69] H. Li, J.A. Peters, Z. Liu, M. Sebastian, C.D. Malliakas, J. Androulakis, L. Zhao, I. Chung, S.L. Nguyen, S. Johnsen, B.W. Wessels, M.G. Kanatzidis, Cryst. Growth Des. 12

(2012) 3250–3256.

[70] V. Grilj, N. Skukan, M. Jakšić, W. Kada, T. Kamiya, Nucl. Instrum. Methods Phys. Res. Sect. B 306 (2013) 191–194.

[71] S.O. Kasap, M.Z. Kabir, K.O. Ramaswami, R.E. Johanson, R.J. Curry, J. Appl. Phys. 128 (2020) 124501.

[72] J. Seco, B. Clasie, M. Partridge, Phys. Med. Biol. 59 (2014) R303–R347.

[73] M. Schieber, H. Hermon, A. Zuck, A. Vilensky, L. Melekhov, R. Shatunovsky, E. Meerson, H. Saado, Nucl. Instrum. Methods Phys. Res. A 458 (2001) 41–46.

[74] A. Mirzaei, J.-S. Huh, S.S. Kim, H.W. Kim, Electron. Mater. Lett. 14 (2018) 261–287.

[75] D.S. McGregor, H. Hermon, Nucl. Instrum. Methods Phys. Res. A 395 (1997) 101–124.

[76] V.M. Sklyarchuk, V.A. Gnatyuk, W. Pecharapa, Nucl. Instrum. Methods Phys. Res. A 879 (2018) 101–105.

[77] T.E. Schlesinger, J.E. Toney, H. Yoon, E.Y. Lee, B.A. Brunett, L. Franks, R.B. James, Mater. Sci. Eng. R Reports 32 (2001) 103–189.

[78] J.M. Holmes, M. Dutta, F.A. Koeck, M.K. Benipal, R. Hathwar, J. Brown, B. Fox, H. Johnson, A. Zaniewski, R. Alarcon, S. Chowdhury, S.M. Goodnick, R.J. Nemanich, Diam. Relat. Mater. 94 (2019) 162–165.

[79] R. Devanathan, L.R. Corrales, F. Gao, W.J. Weber, Nucl. Instrum. Methods Phys. Res. A 565 (2006) 637–649.

[80] M.B. Williams, E.A. Krupinski, K.J. Strauss, W.K. Breeden, M.S. Rzeszotarski, K. Applegate, M. Wyatt, S. Bjork, J.A. Seibert, J. Am. Coll. Radiol. 4 (2007) 371–388.

[81] A. Boora, B. Kaushik, R. Rani, Int. J. Comput. Sci. Eng. Technol. 6 (2016) 115–117.

[82] M.I. Saidaminov, A.L. Abdelhady, B. Murali, E. Alarousu, V.M. Burlakov, W. Peng, I. Dursun, L. Wang, Y. He, G. Maculan, A. Goriely, T. Wu, O.F. Mohammed, O.M. Bakr, Nat. Commun. 6 (2015) 7586.

[83] Y. Zhao, H. Tan, H. Yuan, Z. Yang, J.Z. Fan, J. Kim, O. Voznyy, X. Gong, L.N. Quan, C.S. Tan, J. Hofkens, D. Yu, Q. Zhao, E.H. Sargent, Nat. Commun. 9 (2018) 1607.

[84] W.-G. Li, H.-S. Rao, B.-X. Chen, X.-D. Wang, D.-B. Kuang, J. Mater. Chem. A 5 (2017) 19431–19438.

[85] D. Shi, V. Adinolfi, R. Comin, M. Yuan, E. Alarousu, A. Buin, Y. Chen, S. Hoogland, A. Rothenberger, K. Katsiev, Y. Losovyj, X. Zhang, P.A. Dowben, O.F. Mohammed, E.H. Sargent, O.M. Bakr, Science. 347 (2015) 519–522.

[86] Z. Fan, J. Liu, W. Zuo, G. Liu, X. He, K. Luo, Q. Ye, C. Liao, Phys. Status Solidi A 217 (2020) 2000104.

[87] X. Liu, H. Zhang, B. Zhang, J. Dong, W. Jie, Y. Xu, J. Phys. Chem. C 122 (2018) 14355–14361.

[88] Y. Liu, Z. Yang, D. Cui, X. Ren, J. Sun, X. Liu, J. Zhang, Q. Wei, H. Fan, F. Yu, X. Zhang, C. Zhao, S. Liu, Adv. Mater. 27 (2015) 5176–5183.

[89] Y. Dang, Y. Liu, Y. Sun, D. Yuan, X. Liu, W. Lu, G. Liu, H. Xia, X. Tao, CrystEngComm 17 (2015) 665–670.

[90] Q. Dong, Y. Fang, Y. Shao, P. Mulligan, J. Qiu, L. Cao, J. Huang, Science. 347 (2015) 967–970.

[91] F.P. García de Arquer, A. Armin, P. Meredith, E.H. Sargent, Nat. Rev. Mater. 2 (2017) 16100.

[92] J.H. Heo, D.H. Shin, J.K. Park, D.H. Kim, S.J. Lee, S.H. Im, Adv. Mater. 30 (2018) 1801743.

[93] B. Yang, W. Pan, H. Wu, G. Niu, J.-H. Yuan, K.-H. Xue, L. Yin, X. Du, X.-S. Miao, X. Yang, Q. Xie, J. Tang, Nat. Commun. 10 (2019) 1989.

[94] J. Zhao, L. Zhao, Y. Deng, X. Xiao, Z. Ni, S. Xu, J. Huang, Nat. Photonics 14 (2020) 612–617.

[95] Q. Xu, S. Zhou, J. Huang, X. Ouyang, J. Liu, Y. Guo, J. Wang, J. Nie, X. Zhang, X.

Ouyang, W. Jia, Mater. Today Phys. 18 (2021) 100390.

[96] S.O. Kasap, J.A. Rowlands, Proc. IEEE 90 (2002) 591–604.

[97] H. Grassmann, E. Lorenz, H.-G. Moser, Nucl. Instrum. Methods Phys. Res. A 228 (1985) 323–326.

[98] W. Mengesha, T.D. Taulbee, B.D. Rooney, J.D. Valentine, IEEE Trans. Nucl. Sci. 45 (1998) 456–461.

[99] C.W.E. van Eijk, Nucl. Instrum. Methods Phys. Res. A 509 (2003) 17–25.

[100] J.R. Scheuermann, A.H. Goldan, O. Tousignant, S. Léveillé, W. Zhao, Med. Phys. 42 (2015) 1223–1226.

[101] F. Corsini, G. Griffini, J. Phys. Energy 2 (2020) 031002.

[102] J.G. Rocha, R.A. Dias, L. Goncalves, G. Minas, A. Ferreira, C.M. Costa, S. Lanceros-Mendez, IEEE Sens. J. 9 (2009) 1154–1159.

[103] H. Zhang, G. Dun, Q. Feng, R. Zhao, R. Liang, Z. Gao, T. Hirtz, M. Chen, X. Geng, M. Liu, Y. Huang, X. Zheng, K. Qin, X. Tan, X. Wang, D. Xie, Y. Yang, H. Tian, Y. Zhou, N.P. Padture, X. Wang, J. Hong, T.L. Ren, IEEE Trans. Electron Devices 67 (2020) 3191–3198.

[104] E.V.D. van Loef, P. Dorenbos, C.W.E. van Eijk, K. Krämer, H.U. Güdel, Appl. Phys. Lett. 79 (2001) 1573–1575.

[105] M.D. Birowosuto, P. Dorenbos, J.T.M. de Haas, C.W.E. van Eijk, K.W. Krämer, H.U. Güdel, J. Lumin. 118 (2006) 308–316.

[106] K. Galkowski, A. Mitioglu, A. Miyata, P. Plochocka, O. Portugall, G.E. Eperon, J.T.-W. Wang, T. Stergiopoulos, S.D. Stranks, H.J. Snaith, R.J. Nicholas, Energy Environ. Sci. 9 (2016) 962–970.

[107] V.B. Mykhaylyk, H. Kraus, M. Saliba, Mater. Horizons 6 (2019) 1740–1747.

[108] Y. Li, W. Shao, X. Ouyang, Z. Zhu, H. Zhang, X. Ouyang, B. Liu, Q. Xu, J. Phys. Chem.

C 123 (2019) 17449–17453.

[109] Q. Xu, W. Shao, J. Liu, Z. Zhu, X. Ouyang, J. Cai, B. Liu, B. Liang, Z. Wu, X. Ouyang, ACS Appl. Mater. Interfaces 11 (2019) 47485–47490.

[110] W. Shao, Y. Li, X. Wang, X. Ouyang, J. Cai, C. Li, X. Ouyang, Z. Wu, Q. Xu, Phys. Chem. Chem. Phys. 22 (2020) 6970–6974.

[111] T. Ishihara, J. Takahashi, T. Goto, Solid State Commun. 69 (1989) 933–936.

[112] N. Kawano, M. Koshimizu, G. Okada, Y. Fujimoto, N. Kawaguchi, T. Yanagida, K. Asai, Sci. Rep. 7 (2017) 14754.

[113] A. Horimoto, N. Kawano, D. Nakauchi, H. Kimura, M. Akatsuka, T. Yanagida, Opt. Mater. 101 (2020) 109686.

[114] M. Akatsuka, N. Kawano, T. Kato, D. Nakauchi, G. Okada, N. Kawaguchi, T. Yanagida, Nucl. Instrum. Methods Phys. Res. A 954 (2020) 161372.

[115] A.N. Singh, S. Kajal, J. Kim, A. Jana, J.Y. Kim, K.S. Kim, Adv. Energy Mater. 10 (2020) 2000768.

[116] A. Xie, C. Hettiarachchi, F. Maddalena, M.E. Witkowski, M. Makowski, W. Drozdowski, A. Arramel, A.T.S. Wee, S.V. Springham, P.Q. Vuong, H.J. Kim, C. Dujardin, P. Coquet, M.D. Birowosuto, C. Dang, Commun. Mater. 1 (2020) 37.

[117] F. Maddalena, A. Xie, Arramel, M.E. Witkowski, M. Makowski, B. Mahler, W. Drozdowski, T. Mariyappan, S.V. Springham, P. Coquet, C. Dujardin, M.D. Birowosuto, C. Dang, J. Mater. Chem. C 9 (2021) 2504–2512.

[118] A. Xie, F. Maddalena, M.E. Witkowski, M. Makowski, B. Mahler, W. Drozdowski, S.V. Springham, P. Coquet, C. Dujardin, M.D. Birowosuto, C. Dang, Chem. Mater. 32 (2020) 8530–8539.

[119] A.S. Voloshinovskii, V.B. Mikhailik, S.V. Myagkota, M.S. Pidzyrailo, I.P. Pashuk, Ukr. J. Phys. 38 (1993) 1012–1015.

[120] M. Kobayashi, K. Omata, S. Sugimoto, Y. Tamagawa, T. Kuroiwa, H. Asada, H.

Takeuchi, S. Kondo, Nucl. Instrum. Methods Phys. Res. A 592 (2008) 369–373.

[121] V.B. Mykhaylyk, H. Kraus, V. Kapustianyk, H.J. Kim, P. Mercere, M. Rudko, P. Da Silva, O. Antonyak, M. Dendebera, Sci. Rep. 10 (2020) 8601.

[122] W. Chen, Y. Liu, Z. Yuan, Z. Xu, Z. Zhang, K. Liu, Z. Jin, X. Tang, J. Radioanal. Nucl. Chem. 314 (2017) 2327–2337.

[123] Y. Zhang, R. Sun, X. Ou, K. Fu, Q. Chen, Y. Ding, L.-J. Xu, L. Liu, Y. Han, A. V. Malko, X. Liu, H. Yang, O.M. Bakr, H. Liu, O.F. Mohammed, ACS Nano 13 (2019) 2520–2525.

[124] K. Watanabe, M. Koshimizu, T. Yanagida, Y. Fujimoto, K. Asai, Jpn. J. Appl. Phys. 55 (2016) 02BC20.

[125] F. Cao, D. Yu, W. Ma, X. Xu, B. Cai, Y.M. Yang, S. Liu, L. He, Y. Ke, S. Lan, K.-L. Choy, H. Zeng, ACS Nano 14 (2020) 5183–5193.

[126] Q. Xu, J. Wang, W. Shao, X. Ouyang, X. Wang, X. Zhang, Y. Guo, X. Ouyang, Nanoscale 12 (2020) 9727–9732.

[127] Q. Hu, Z. Deng, M. Hu, A. Zhao, Y. Zhang, Z. Tan, G. Niu, H. Wu, J. Tang, Sci. China Chem. 61 (2018) 1581–1586.

[128] W. Zhu, W. Ma, Y. Su, Z. Chen, X. Chen, Y. Ma, L. Bai, W. Xiao, T. Liu, H. Zhu, X. Liu, H. Liu, X. Liu, Y. Yang, Light Sci. Appl. 9 (2020) 112.

[129] J. Cao, Z. Guo, S. Zhu, Y. Fu, H. Zhang, Q. Wang, Z. Gu, ACS Appl. Mater. Interfaces 12 (2020) 19797–19804.

[130] Z. Wang, X. Xu, S. Wang, H. Xu, W. Xu, Q. Zeng, G. Deng, Y. Jiang, S.-F. Wu, Chem. – A Eur. J. 27 (2021) 9071–9076.

[131] C. Zhou, L. -J. Xu, S. Lee, H. Lin, B. Ma, Adv. Opt. Mater. 9 (2021) 2001766.

[132] V. Morad, Y. Shynkarenko, S. Yakunin, A. Brumberg, R.D. Schaller, M. V. Kovalenko, J. Am. Chem. Soc. 141 (2019) 9764–9768.

[133] Q. He, C. Zhou, L. Xu, S. Lee, X. Lin, J. Neu, M. Worku, M. Chaaban, B. Ma, ACS

Mater. Lett. 2 (2020) 633–638.

[134] L.-J. Xu, X. Lin, Q. He, M. Worku, B. Ma, Nat. Commun. 11 (2020) 4329.

[135] Y. Wu, D. Han, B.C. Chakoumakos, H. Shi, S. Chen, M.-H. Du, I. Greeley, M. Loyd, D.J. Rutstrom, L. Stand, M. Koschan, C.L. Melcher, J. Mater. Chem. C 6 (2018) 6647–6655.

[136] B. Yang, L. Yin, G. Niu, J. Yuan, K. Xue, Z. Tan, X. Miao, M. Niu, X. Du, H. Song, E. Lifshitz, J. Tang, Adv. Mater. 31 (2019) 1904711.

[137] W. Gao, G. Niu, L. Yin, B. Yang, J.-H. Yuan, D. Zhang, K.-H. Xue, X. Miao, Q. Hu, X. Du, J. Tang, ACS Appl. Electron. Mater. 2 (2020) 2242–2249.

[138] X. Zhao, G. Niu, J. Zhu, B. Yang, J.-H. Yuan, S. Li, W. Gao, Q. Hu, L. Yin, K.-H. Xue, E. Lifshitz, X. Miao, J. Tang, J. Phys. Chem. Lett. 11 (2020) 1873–1880.

[139] S. Cheng, A. Beitlerova, R. Kucerkova, M. Nikl, G. Ren, Y. Wu, Phys. Status Solidi – Rapid Res. Lett. 14 (2020) 2000374.

[140] L. Lian, M. Zheng, W. Zhang, L. Yin, X. Du, P. Zhang, X. Zhang, J. Gao, D. Zhang, L. Gao, G. Niu, H. Song, R. Chen, X. Lan, J. Tang, J. Zhang, Adv. Sci. 7 (2020) 2000195.

[141] J.-H. Wei, J.-F. Liao, X.-D. Wang, L. Zhou, Y. Jiang, D.-B. Kuang, Matter 3 (2020) 892–903.

[142] T.S. Sherkar, C. Momblona, L. Gil-Escrig, J. Ávila, M. Sessolo, H.J. Bolink, L.J.A. Koster, ACS Energy Lett. 2 (2017) 1214–1222.

[143] X. Zheng, B. Chen, J. Dai, Y. Fang, Y. Bai, Y. Lin, H. Wei, X.C. Zeng, J. Huang, Nat. Energy 2 (2017) 17102.

[144] M. Hu, S. Jia, Y. Liu, J. Cui, Y. Zhang, H. Su, S. Cao, L. Mo, D. Chu, G. Zhao, K. Zhao, Z. Yang, S.F. Liu, ACS Appl. Mater. Interfaces 12 (2020) 16592–16600.

[145] L. Basiricò, S.P. Senanayak, A. Ciavatti, M. Abdi-Jalebi, B. Fraboni, H. Sirringhaus, Adv. Funct. Mater. 29 (2019) 1902346.

[146] Y. Huang, L. Qiao, Y. Jiang, T. He, R. Long, F. Yang, L. Wang, X. Lei, M. Yuan, J.

Chen, Angew. Chemie Int. Ed. 58 (2019) 17834–17842.

[147] H. Mescher, F. Schackmar, H. Eggers, T. Abzieher, M. Zuber, E. Hamann, T. Baumbach, B.S. Richards, G. Hernandez-Sosa, U.W. Paetzold, U. Lemmer, ACS Appl. Mater. Interfaces 12 (2020) 15774–15784.

[148] W. Wang, H. Meng, H. Qi, H. Xu, W. Du, Y. Yang, Y. Yi, S. Jing, S. Xu, F. Hong, J. Qin, J. Huang, Z. Xu, Y. Zhu, R. Xu, J. Lai, F. Xu, L. Wang, J. Zhu, Adv. Mater. 32 (2020) 2001540.

[149] Y. He, W. Ke, G.C.B. Alexander, K.M. McCall, D.G. Chica, Z. Liu, I. Hadar, C.C. Stoumpos, B.W. Wessels, M.G. Kanatzidis, ACS Photonics 5 (2018) 4132–4138.

[150] F. Yao, J. Peng, R. Li, W. Li, P. Gui, B. Li, C. Liu, C. Tao, Q. Lin, G. Fang, Nat. Commun. 11 (2020) 1194.

[151] J. Song, X. Feng, H. Li, W. Li, T. Lu, C. Guo, H. Zhang, H. Wei, B. Yang, J. Phys. Chem. Lett. 11 (2020) 3529–3535.

[152] Q. Xu, W. Shao, Y. Li, X. Zhang, X. Ouyang, J. Liu, B. Liu, Z. Wu, X. Ouyang, X. Tang, W. Jia, ACS Appl. Mater. Interfaces 11 (2019) 9679–9684.

[153] L. Li, X. Liu, H. Zhang, B. Zhang, W. Jie, P.J. Sellin, C. Hu, G. Zeng, Y. Xu, ACS Appl. Mater. Interfaces 11 (2019) 7522–7528.

[154] F. Ye, H. Lin, H. Wu, L. Zhu, Z. Huang, D. Ouyang, G. Niu, W.C.H. Choy, Adv. Funct. Mater. 29 (2019) 1806984.

[155] Y. Song, L. Li, W. Bi, M. Hao, Y. Kang, A. Wang, Z. Wang, H. Li, X. Li, Y. Fang, D. Yang, Q. Dong, Research 2020 (2020) 5958243.

[156] Y. Huang, L. Qiao, Y. Jiang, T. He, R. Long, F. Yang, L. Wang, X. Lei, M. Yuan, J. Chen, Angew. Chemie Int. Ed. 58 (2019) 17834–17842.

[157] S. Tian, F. Sui, K. He, G. Cheng, Y. Ge, D. Ning, Z. Wang, Z. Wang, G. Tao, Z. Wang, B. Du, L. Wei, W. Li, C. Yang, M. Chen, Nano Energy 78 (2020) 105335.

[158] X. Geng, Q. Feng, R. Zhao, T. Hirtz, G. Dun, Z. Yan, J. Ren, H. Zhang, R. Liang, H. Tian,

D. Xie, Y. Yang, T.-L. Ren, IEEE Electron Device Lett. 41 (2020) 256–259.

[159] X. Wang, D. Zhao, Y. Qiu, Y. Huang, Y. Wu, G. Li, Q. Huang, Q. Khan, A. Nathan, W. Lei, J. Chen, Phys. Status Solidi RRL 12 (2018) 1800380.

[160] G.J. Matt, I. Levchuk, J. Knüttel, J. Dallmann, A. Osvet, M. Sytnyk, X. Tang, J. Elia, R. Hock, W. Heiss, C.J. Brabec, Adv. Mater. Interfaces 7 (2020) 1901575.

[161] Z. Gou, S. Huanglong, W. Ke, H. Sun, H. Tian, X. Gao, X. Zhu, D. Yang, P. Wangyang, Phys. Status Solidi – Rapid Res. Lett. 13 (2019) 1900094.

[162] Y. Haruta, T. Ikenoue, M. Miyake, T. Hiratol, MRS Adv. 5 (2020) 395–401.

[163] W. Pan, B. Yang, G. Niu, K.-H. Xue, X. Du, L. Yin, M. Zhang, H. Wu, X.-S. Miao, J. Tang, Adv. Mater. 31 (2019) 1904405.

[164] Q. Xu, X. Wang, H. Zhang, W. Shao, J. Nie, Y. Guo, J. Wang, X. Ouyang, ACS Appl. Electron. Mater. 2 (2020) 879–884.

[165] J. Liu, B. Shabbir, C. Wang, T. Wan, Q. Ou, P. Yu, A. Tadich, X. Jiao, D. Chu, D. Qi, D. Li, R. Kan, Y. Huang, Y. Dong, J. Jasieniak, Y. Zhang, Q. Bao, Adv. Mater. 31 (2019) 1901644.

[166] B.-B. Zhang, X. Liu, B. Xiao, A.B. Hafsia, K. Gao, Y. Xu, J. Zhou, Y. Chen, J. Phys. Chem. Lett. 11 (2020) 432–437.

[167] Z. Zhang, C.C. Chung, Z. Huang, E. Vetter, D. Seyitliyev, D. Sun, K. Gundogdu, F.N. Castellano, E.O. Danilov, G. Yang, Mater. Lett. 269 (2020) 127667.

[168] J.A. Steele, W. Pan, C. Martin, M. Keshavarz, E. Debroye, H. Yuan, S. Banerjee, E. Fron, D. Jonckheere, C.W. Kim, W. Baekelant, G. Niu, J. Tang, J. Vanacken, M. Van der Auweraer, J. Hofkens, M.B.J. Roeffaers, Adv. Mater. 30 (2018) 1804450.

[169] H. Zhang, Y. Yang, X. Wang, T.-L. Ren, Z. Gao, R. Liang, X. Zheng, X. Geng, Y. Zhao, D. Xie, J. Hong, H. Tian, IEEE Trans. Electron Devices 66 (2019) 2224–2229.

[170] L. Yin, H. Wu, W. Pan, B. Yang, P. Li, J. Luo, G. Niu, J. Tang, Adv. Opt. Mater. 7 (2019) 1900491.

[171] H. Li, X. Shan, J.N. Neu, T. Geske, M. Davis, P. Mao, K. Xiao, T. Siegrist, Z. Yu, J. Mater. Chem. C 6 (2018) 11961–11967.

[172] Q. Sun, Y. Xu, H. Zhang, B. Xiao, X. Liu, J. Dong, Y. Cheng, B. Zhang, W. Jie, M.G. Kanatzidis, J. Mater. Chem. A 6 (2018) 23388–23395.

[173] M. Xia, J. Yuan, G. Niu, X. Du, L. Yin, W. Pan, J. Luo, Z. Li, H. Zhao, K. Xue, X. Miao, J. Tang, Adv. Funct. Mater. 30 (2020) 1910648.

[174] R. Zhuang, X. Wang, W. Ma, Y. Wu, X. Chen, L. Tang, H. Zhu, J. Liu, L. Wu, W. Zhou, X. Liu, Y. (Michael) Yang, Nat. Photonics 13 (2019) 602–608.

[175] S. Tie, W. Zhao, D. Xin, M. Zhang, J. Long, Q. Chen, X. Zheng, J. Zhu, W. Zhang, Adv. Mater. 32 (2020) 2001981.

[176] Y. Liu, Y. Zhang, Z. Yang, J. Cui, H. Wu, X. Ren, K. Zhao, J. Feng, J. Tang, Z. Xu, S. (Frank) Liu, Adv. Opt. Mater. 8 (2020) 2000814.

[177] X. Zheng, W. Zhao, P. Wang, H. Tan, M.I. Saidaminov, S. Tie, L. Chen, Y. Peng, J. Long, W.H. Zhang, J. Energy Chem. 49 (2020) 299–306.

[178] Y. Liu, Z. Xu, Z. Yang, Y. Zhang, J. Cui, Y. He, H. Ye, K. Zhao, H. Sun, R. Lu, M. Liu, M.G. Kanatzidis, S. (Frank) Liu, Matter 3 (2020) 180–196.

[179] L. Yao, G. Niu, L. Yin, X. Du, Y. Lin, X. Den, J. Zhang, J. Tang, J. Mater. Chem. C 8 (2020) 1239–1243.

[180] Y. Shen, Y. Liu, H. Ye, Y. Zheng, Q. Wei, Y. Xia, Y. Chen, K. Zhao, W. Huang, S. (Frank) Liu, Angew. Chemie Int. Ed. 59 (2020) 14896–14902.

[181] H. Li, J. Song, W. Pan, D. Xu, W. Zhu, H. Wei, B. Yang, Adv. Mater. 32 (2020) 2003790.

[182] C. Ji, S. Wang, Y. Wang, H. Chen, L. Li, Z. Sun, Y. Sui, S. Wang, J. Luo, Adv. Funct. Mater. 30 (2020) 1905529.

[183] X. Song, Q. Cui, Y. Liu, Z. Xu, H. Cohen, C. Ma, Y. Fan, Y. Zhang, H. Ye, Z. Peng, R. Li, Y. Chen, J. Wang, H. Sun, Z. Yang, Z. Liu, Z. Yang, W. Huang, G. Hodes, S. (Frank) Liu, K. Zhao, Adv. Mater. 32 (2020) 2003353.

[184] D.B. Mitzi, D.R. Medeiros, P.W. DeHaven, Chem. Mater. 14 (2002) 2839–2841.

[185] X. Liu, T. Xu, Y. Li, Z. Zang, X. Peng, H. Wei, W. Zha, F. Wang, Sol. Energy Mater. Sol. Cells 187 (2018) 249–254.

[186] A.H. Slavney, T. Hu, A.M. Lindenberg, H.I. Karunadasa, J. Am. Chem. Soc. 138 (2016) 2138–2141.

[187] W. Yuan, G. Niu, Y. Xian, H. Wu, H. Wang, H. Yin, P. Liu, W. Li, J. Fan, Adv. Funct. Mater. 29 (2019) 1900234.

[188] Z. Xu, X. Liu, Y. Li, X. Liu, T. Yang, C. Ji, S. Han, Y. Xu, J. Luo, Z. Sun, Angew. Chemie Int. Ed. 58 (2019) 15757–15761.

[189] A. Jana, S. Park, S. Cho, H. Kim, H. Im, Matter 5 (2022) 20–22.

[190] E.M. Pogson, J. McNamara, P. Metcalfe, R.A. Lewis, Quant. Imaging Med. Surg. 3 (2013) 18–27.

[191] Y. Rong, Y. Ming, W. Ji, D. Li, A. Mei, Y. Hu, H. Han, J. Phys. Chem. Lett. 9 (2018) 2707–2713.

[192] T. Matsushima, T. Fujihara, C. Qin, S. Terakawa, Y. Esaki, S. Hwang, A.S.D. Sandanayaka, W.J. Potscavage, C. Adachi, J. Mater. Chem. A 3 (2015) 17780–17787.

[193] T. Li, A.M. Zeidell, G. Findik, W.A. Dunlap-Shohl, J. Euvrard, K. Gundogdu, O.D. Jurchescu, D.B. Mitzi, Chem. Mater. 31 (2019) 4267–4274.

[194] R.L. Sheffield, C.W. Barnes, J.P. Tapia, Proc. 38th Int. Free. Laser Conf. FEL 2017 (2017) 24–28.

Graphical Abstract